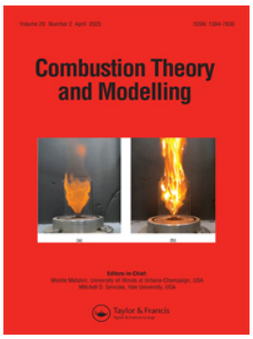

Taylor & Francis
Taylor & Francis Group

Combustion Theory and Modelling

ISSN: (Print) (Online) Journal homepage: www.tandfonline.com/journals/tctm20

Linear quadrature method of moments for solving the transported probability density function model for turbulent combustion

Yunchu Wang, Yize Wang & Li Yuan

To cite this article: Yunchu Wang, Yize Wang & Li Yuan (2025) Linear quadrature method of moments for solving the transported probability density function model for turbulent combustion, Combustion Theory and Modelling, 29:2, 145-176, DOI: 10.1080/13647830.2025.2463893

To link to this article: https://doi.org/10.1080/13647830.2025.2463893

Combustion Theory and Modelling, 2025
Vol. 29, No. 2, 145–176, https://doi.org/10.1080/13647830.2025.2463893

Linear quadrature method of moments for solving the transported probability density function model for turbulent combustion

Yunchu Wang[a,b], Yize Wang[a,b] and Li Yuan[a,b*]

[a]*ICMSEC & LSEC, Academy of Mathematics and Systems Science, Chinese Academy of Sciences, Beijing, People's Republic of China* [b]*School of Mathematical Sciences, University of Chinese Academy of Sciences, Beijing, People's Republic of China*

(*Received 6 February 2024; accepted 26 January 2025*)

Large eddy simulation (LES) coupled with the transported probability density function (PDF) model has become a promising strategy for modelling turbulent combustion. For solving the high-dimensional PDF transport equation numerically, deterministic quadrature-based moment methods have arisen as an alternative choice besides stochastic particle and stochastic field methods. In this work, we propose a new quadrature-based moment method called linear Quadrature Method Of Moments (LQMOM) for the univariate PDF case. This method assumes that the underlying PDF distribution is smooth and it uses a set of predefined quadrature nodes and weights in the sample space to establish a linear system of equations for the PDF values at the quadrature nodes from the moments. The LQMOM is more efficient than the original QMOM which needs to solve a nonlinear system of equations for the moment inversion. However, it may generate negative PDF values for non-smooth PDF distributions. To remedy this flaw, we construct the LQMOM-QMOM hybrid algorithm by using detectors to detect single- and two-peak distributions. Furthermore, we extend the LQMOM to the multivariate PDF case by utilizing the main idea of the conditional QMOM (CQMOM) to obtain the linear CQMOM (LCQMOM), and then reduce it to the simplified version (LCQMOM-S) to gain efficiency. The LQMOM-QMOM hybrid algorithm for univariate PDFs is tested in a typical example and the LCQMOM-S-CQMOM hybrid algorithm for multivariate PDFs is checked in compressible turbulent reactive 2D shear layer flow and 3D air/H_2 jet. It is shown that the hybrid algorithms can reduce 20–35% simulation time and produce similar results compared with the respective QMOM and CQMOM.

Keywords: turbulent combustion; large eddy simulation; probability density function; quadrature-based moment method; linear inversion; hybrid algorithm

1. Introduction

Turbulent combustion is an interdisciplinary research topic across fluid mechanics, engineering thermophysics, and chemical kinetics [1–3]. The flow turbulence, fuel atomization, interaction between flow turbulence and chemical reactions, heat transfer and soot formation, etc, greatly increase the difficulty of research on turbulent combustion. Nowadays large eddy simulation (LES) has become a popular method for studying turbulent combustion [4,5]. LES is usually implemented with a turbulent combustion model for defining a suitable representation of the mean reaction rates. Commonly used combustion models include the flamelet model [6], transported probability density function (PDF)

*Corresponding author. Email: lyuan@lsec.cc.ac.cn

model [7–10], conditional moment closure model [11,12], linear eddy model [13,14], and thickened flame model [15–17], to name a few.

The hybrid LES/PDF method has been found to be highly effective for modelling turbulent reacting flows [7–10,18–20] albeit with a high computational cost. The LES part solves the hydrodynamic equations to provide the filtered velocity field and the turbulent diffusivity to the PDF part. In the PDF part, a set of thermo-chemical variables (called compositions) are represented in terms of a one-point one-time joint probability density function which provides all the information for calculating the filtered compositions and the filtered chemical reaction rates required by the LES part. The joint PDF is governed by a high-dimensional (time, space, and compositions) transport equation. The chemical reaction source terms in this equation are in a closed form, which is the main advantage of the PDF turbulent combustion model [7].

Traditional numerical methods like finite volume methods cannot be used to solve the PDF transport equation due to the curse of dimensionality. Usually, stochastic methods are more effective for the numerical approximation of the PDF equation. Two kinds of stochastic methods, the Lagrangian Monte Carlo (MC) particle methods [7,9,20–23] and the Eulerian stochastic field methods [24–27], have been successfully applied to low Mach number turbulent combustion problems with the former kind being more popular. However, for high Mach number problems with shocks, the MC particle methods may generate significant statistical fluctuations across shocks and even lead to numerical instability [28]. Besides, stochastic methods must have enough number of notional particles/stochastic fields in each grid cell to reduce the statistical error to a reasonable tolerance, which may incur a high computational cost.

An alternative, deterministic Eulerian approach for solving a high-dimensional PDF equation is the quadrature-based moment methods (QBMMs) [29,30]. The main idea of QBMM is to solve the moment transport equations of the PDF, and then use the moments to reconstruct the PDF distribution (called moment inversion process) for the closure of chemical reaction source terms or other nonlinear source terms in the moment transport equations. There are different variants of QBMMs. In the original quadrature method of moments (QMOM) [29], the PDF is approximated by the weighted sum of a finite number of Dirac delta functions. The weights and abscissas of the Dirac delta functions are inverted and then used for the closure of the source terms which cannot be expressed in terms of the moments. Base on the QMOM, the extended quadrature method of moments (EQMOM) [31] and conditional quadrature method of moments (CQMOM) [32,33] were developed for the population balance equation (PBE) describing discrete particles in a carrier fluid with aggregation and breakup, and evaporation and condensation processes. These methods can achieve good accuracy, but the moment inversion process is expensive. On the other hand, the direct quadrature method of moments (DQMOM) [30,34] solves the transport equations for the weights and weighted abscissas, which avoids the moment inversion. This method has been applied to solving the PBE [33] and simulating turbulent reacting flows [34,35]. However, the weights and abscissas are not conserved quantities, which will lead to low accuracy in non-premixed combustion. Later, the semi-discrete quadrature method of moments (SeQMOM) [28,36] was developed in which the weight and moment transport equations are solved and Jacobian matrices are used to convert the time changes of weights and of moments to the time change of weighted abscissas. The SeQMOM combines the advantages of QMOM and DQMOM, but it cannot work well if the Jacobian matrix is ill-conditioned, and does not guarantee the physical bounds.

In this work, a new QBMM called linear quadrature method of moments (LQMOM) is developed. The unknown PDF distribution is assumed to be smooth and thus the moments as integrals in the composition space are approximated by a quadrature rule with a set of predefined quadrature nodes and weights. In this way, a linear system of equations are established for the PDF values at the quadrature nodes. Therefore, the moment inversion process only needs to solve a linear system of equations, which can reduce the computational cost. However, when the underlying PDF distribution is not smooth like a weighted sum of Dirac delta functions, the LQMOM may return negative PDF values. To remedy this flaw, we construct a hybrid LQMOM-QMOM algorithm by using a switch function based on the one- and two-peak distribution detectors. Further, in order to extend the LQMOM to the multivariate PDF case for modelling multi-species reactive flows, we refer to the idea of the CQMOM [33] and construct the linear CQMOM (LCQMOM) and its simplified version, LCQMOM-S.

The rest of the paper is organised as follows. In Section 2, the governing equations for the LES/PDF method and the QMOM are reviewed. In Section 3, the LQMOM for the univariate PDF case is proposed and then tested in some simple examples. In Section 4, the two detectors and the LQMOM-QMOM hybrid algorithm are designed. in Section 5, the LQMOM is extended to the multivariate PDF case to get the LCQMOM and LCQMOM-S as well as the hybrid algorithm. In Section 6, the reacting shear layer and air-hydrogen jet problems are used to test the effectiveness of the proposed hybrid algorithms. Finally, conclusions are given in Section 7.

2. LES/PDF hybrid method and quadrature method of moments

2.1. *Governing equations for LES/PDF hybrid method*

In the framework of LES, the filtering of a quantity Q is defined as

$$\overline{Q}(\mathbf{x},t)=\int_{-\infty}^{\infty}Q(\mathbf{x}',t)G_{\Delta}(\mathbf{x}'-\mathbf{x})\mathrm{d}\mathbf{x}', \tag{1}$$

where $G_{\Delta}(\mathbf{y})$ is the filter function with the filter width Δ. For variable density flows, the Favre filtering or density-weighted filtering is preferred, which is defined as

$$\tilde{Q}(\mathbf{x},t)=\frac{\overline{\rho Q}(\mathbf{x},t)}{\overline{\rho}(\mathbf{x},t)}, \tag{2}$$

where $\rho(\mathbf{x},t)$ is the fluid density. Applying the filter to the compressible reactive Navier–Stokes equations for a gas mixture composed of N_s species, we can obtain

$$\begin{aligned}
&\frac{\partial\overline{\rho}}{\partial t}+\frac{\partial(\overline{\rho}\tilde{u}_i)}{\partial x_i}=0,\\
&\frac{\partial(\overline{\rho}\tilde{u}_j)}{\partial t}+\frac{\partial(\overline{\rho}\tilde{u}_i\tilde{u}_j)}{\partial x_i}=-\frac{\partial\overline{p}}{\partial x_j}+\frac{\partial\overline{\tau}_{ij}}{\partial x_i}-\frac{\partial\tau_{ij}^{\mathrm{sgs}}}{\partial x_i},\\
&\frac{\partial(\overline{\rho}\tilde{E})}{\partial t}+\frac{\partial\left(\tilde{u}_i(\overline{\rho}\tilde{E}+\overline{p})\right)}{\partial x_i}=-\frac{\partial\tilde{q}_i}{\partial x_i}+\frac{\partial(\tilde{u}_j\tilde{\tau}_{ij})}{\partial x_i}-\frac{\partial\mathcal{E}_i^{\mathrm{sgs}}}{\partial x_i},\\
&\frac{\partial(\overline{\rho}\tilde{Y}_{\alpha})}{\partial t}+\frac{\partial(\overline{\rho}\tilde{u}_i\tilde{Y}_{\alpha})}{\partial x_i}=-\frac{\partial\tilde{J}_{i,\alpha}}{\partial x_i}+\overline{\rho}\tilde{\dot{\omega}}_{\alpha}-\frac{\partial\mathcal{Y}_{i,\alpha}^{\mathrm{sgs}}}{\partial x_i},\quad \alpha=1,\ldots,N_s-1,
\end{aligned} \tag{3}$$

where $\tilde{u}_i$, $\tilde{E}$, and $\tilde{Y}_\alpha$ are the Favre filtered velocities, total energy, and mass fractions, respectively. The filtered pressure $\overline{p}$ is calculated from the equation of state as $\overline{p} = \overline{\rho}\tilde{R}\tilde{T}$, where the mixture gas constant is defined as $\tilde{R} = \sum_{\alpha=1}^{N_s} \tilde{Y}_\alpha R_\alpha$, and the temperature $\tilde{T}$ is iteratively calculated from the basic thermodynamical relation, $h(\tilde{Y}_1, \ldots, \tilde{Y}_{N_s}, \tilde{T}) = \tilde{E} - \frac{1}{2}\tilde{u}_i\tilde{u}_i + \tilde{R}\tilde{T}$, where h is the mixture enthalpy. The filtered shear stress tensor $\overline{\tau}_{ij}$, the resoled heat flux $\tilde{q}_i$, species diffusion flux $\tilde{J}_{i,\alpha}$, and shear stress work $\tilde{u}_j\tilde{\tau}_{ij}$, are determined by the respective laminar formulas with the resolved variables,

$$\overline{\tau}_{ij} \approx \tilde{\tau}_{ij} = 2\tilde{\mu}\left(\tilde{S}_{ij} - \frac{1}{3}\delta_{ij}\frac{\partial \tilde{u}_k}{\partial x_k}\right), \quad \text{where } \tilde{S}_{ij} = \frac{1}{2}\left(\frac{\partial \tilde{u}_i}{\partial x_j} + \frac{\partial \tilde{u}_j}{\partial x_i}\right), \tag{4}$$

$$\tilde{q}_i = -\tilde{\lambda}\frac{\partial \tilde{T}}{\partial x_i} - \sum_{\alpha=1}^{N_s} \tilde{h}_\alpha \overline{\rho}\tilde{D}_\alpha \frac{\partial \tilde{Y}_\alpha}{\partial x_i}, \tag{5}$$

$$\tilde{J}_{i,\alpha} = -\overline{\rho}\tilde{D}_\alpha \frac{\partial \tilde{Y}_\alpha}{\partial x_i}. \tag{6}$$

Here, $\tilde{\mu} = \mu(\tilde{T})$, $\tilde{\lambda} = \lambda(\tilde{T})$, $\tilde{D}_\alpha = D_\alpha(\tilde{T})$, and $\tilde{h}_\alpha = h_\alpha(\tilde{T})$ are the molecular viscosity, thermal conductivity, species diffusivity, and species enthalpy respectively.

The subgrid scale (SGS) stress tensor is modelled using the Smagorinsky model [37,38] as

$$\tau_{ij}^{\text{sgs}} := \overline{\rho}\widetilde{u_i u_j} - \overline{\rho}\tilde{u}_i\tilde{u}_j = -2\overline{\rho}\nu_t\left(\tilde{S}_{ij} - \frac{1}{3}\delta_{ij}\frac{\partial \tilde{u}_k}{\partial x_k}\right) + \frac{1}{3}\delta_{ij}\tau_{kk}^{\text{sgs}}, \tag{7}$$

where $\nu_t = (C_S\Delta)^2|2\tilde{S}_{ij}\tilde{S}_{ij}|^{1/2}$ is the subgrid scale viscosity, Δ is the filter width usually set to the representative mesh size, and C_S is the model parameter. The sum of the SGS convective total enthalpy flux, heat flux, and shear stress work, $\mathcal{E}_i^{\text{sgs}}$, and the sum of the SGS species convective flux and diffusive flux, $\mathcal{Y}_{i,\alpha}^{\text{sgs}}$, are modelled as [39]

$$\begin{aligned}
\mathcal{E}_i^{\text{sgs}} &:= \left(\overline{u_i(\rho E + p)} - \tilde{u}_i(\overline{\rho}\tilde{E} + \overline{p})\right) + \left(\overline{q}_i - \tilde{q}_i\right) - \left(\overline{u_j\tau_{ij}} - \tilde{u}_j\tilde{\tau}_{ij}\right) \\
&\approx -\lambda_t\frac{\partial \tilde{T}}{\partial x_i} - \sum_{\alpha=1}^{N_s}\tilde{h}_\alpha\overline{\rho}D_t\frac{\partial \tilde{Y}_\alpha}{\partial x_i} + \tilde{u}_j\tau_{ij}^{\text{sgs}}, \\
\mathcal{Y}_{i,\alpha}^{\text{sgs}} &:= \left(\overline{\rho}\widetilde{u_i Y_\alpha} - \overline{\rho}\tilde{u}_i\tilde{Y}_\alpha\right) + \left(\overline{J}_{i,\alpha} - \tilde{J}_{i,\alpha}\right) \approx -\overline{\rho}D_t\frac{\partial \tilde{Y}_\alpha}{\partial x_i},
\end{aligned}$$

where λ_t is the turbulent thermal conductivity and D_t the turbulent mass diffusivity.

The chemical reaction rate $\dot{\omega}_\alpha$ is a nonlinear function of species concentrations and thermodynamic variables. The modelling of the filtered chemical reaction rate $\tilde{\dot{\omega}}_\alpha$ in Equation (3) is accomplished by using the PDF method as described below.

For compressible turbulent reactive flows, the filtered mass density function (FMDF) [9] is preferred and is defined as

$$F(\boldsymbol{\psi}; \mathbf{x}, t) = \int_{-\infty}^{\infty} \rho(\mathbf{x}', t)\xi\left(\boldsymbol{\psi} - \boldsymbol{\phi}(\mathbf{x}', t)\right) G_\Delta(\mathbf{x}' - \mathbf{x})\mathrm{d}\mathbf{x}', \tag{8}$$

where $\boldsymbol{\phi} = (\phi_1, \ldots, \phi_{N_s}) = (Y_1, \ldots, Y_{N_s-1}, h)$ is a random vector composed of the species mass fractions Y_α and mixture enthalpy h, $\boldsymbol{\psi}$ is the sample space corresponding to $\boldsymbol{\phi}$,

$\xi(\boldsymbol{\psi}-\boldsymbol{\phi}(\mathbf{x},t))=\prod_{\alpha=1}^{N_s}\delta(\psi_\alpha-\phi_\alpha(\mathbf{x},t))$ is the 'fine grained' density function, and δ is the Dirac delta function. The transport equation for $F(\boldsymbol{\psi};\mathbf{x},t)$ can be derived from the conservation equations of species mass and mixture enthalpy [9,10]. In particular, under the assumption of equal diffusivity $D_\alpha\equiv D,\forall\alpha$ and unit Lewis number, and using the interaction by exchange with the mean (IEM) model [9,28] for the conditional diffusion terms of the mass and heat and the gradient model for the conditional convection term, the PDF transport equation can be written as the form:

$$\frac{\partial F}{\partial t}+\frac{\partial\left(\tilde{u}_i F\right)}{\partial x_i}=\frac{\partial}{\partial x_i}\left[\overline{\rho}(D+D_t)\frac{\partial(F/\overline{\rho})}{\partial x_i}\right]+\frac{\partial}{\partial\psi_\alpha}\left[\Omega(\psi_\alpha-\tilde{\phi}_\alpha)F\right]-\frac{\partial}{\partial\psi_\alpha}\left[\overline{S_\alpha|\boldsymbol{\psi}}F\right], \tag{9}$$

where the repeated indices i and α indicate summation over all the relevant dimensions. The source terms $\overline{S_\alpha|\boldsymbol{\psi}}=\dot{\omega}_\alpha(\boldsymbol{\psi})|\boldsymbol{\psi}=\dot{\omega}_\alpha(\boldsymbol{\psi})$, $1\le\alpha\le N_s-1$ represent the species mass production rates due to chemical reactions. Note that these terms are in a closed form, which is the main advantage of the PDF method. However, the enthalpy source term $\overline{S_\alpha=S_h|\boldsymbol{\psi}}$, $\alpha=N_s$ is not closed. It includes the effects of pressure material derivative, viscous dissipation, and their SGS components. We ignore the pressure fluctuation and the SGS component of the viscous dissipation as done by [27,28], thus

$$\overline{S_{N_s}|\boldsymbol{\psi}}=\overline{S_h|\boldsymbol{\psi}}=\overline{\frac{1}{\rho}\left(\frac{Dp}{Dt}+\tau_{ij}\frac{\partial u_j}{\partial x_i}\right)|\boldsymbol{\psi}}\approx\frac{1}{\overline{\rho}}\left(\frac{D\overline{p}}{Dt}+\tilde{\tau}_{ij}\frac{\partial\tilde{u}_j}{\partial x_i}\right). \tag{10}$$

The filtered compositions and the mixing frequency in Equation (9) are given by

$$\tilde{\phi}_\alpha(\mathbf{x},t)=\frac{1}{\overline{\rho}(\mathbf{x},t)}\int_{-\infty}^{\infty}\psi_\alpha F(\boldsymbol{\psi};\mathbf{x},t)\mathrm{d}\boldsymbol{\psi},\quad \Omega=C_\Omega\frac{D+D_t}{\Delta^2},\quad C_\Omega=2.0\ \text{(as [28])}.$$

2.2. *Quadrature method of moments* (*QMOM*)

Since the PDF equation (9) is high-dimensional, Lagrangian Monte Carlo particle methods (cf. [7]) or Eulerian stochastic field methods (cf. [24]) are often employed to solve it. Recently, QBMMs were also applied to solve Equation (9) [28,34]. As the original QMOM [29] is the basis of QBMMs, we briefly introduce it in this subsection.

The main idea of the QMOM is to solve a finite number of moment transport equations and use the moments to reconstruct an approximate PDF represented by a set of weighted Dirac delta functions centred at quadrature nodes in the sample space. Define the (unmixed) moments of the joint PDF $f(\boldsymbol{\psi};\mathbf{x},t):=F/\overline{\rho}$ as (we take unmixed moments as an example; mixed moments can be defined similarly)

$$M_{n,\alpha}(\mathbf{x},t)=\int_{-\infty}^{\infty}\psi_\alpha^n f(\boldsymbol{\psi};\mathbf{x},t)\mathrm{d}\boldsymbol{\psi}=\frac{1}{\overline{\rho}}\int_{-\infty}^{\infty}\psi_\alpha^n F(\boldsymbol{\psi};\mathbf{x},t)\mathrm{d}\boldsymbol{\psi}, \tag{11}$$

where the moment orders n are typically non-negative integers. The moment transport equations can be obtained by multiplying Equation (9) with ψ_β^n and integration,

$$\frac{\partial\left(\overline{\rho}M_{n,\beta}\right)}{\partial t}+\frac{\partial\left(\overline{\rho}\tilde{u}_i M_{n,\beta}\right)}{\partial x_i}=\frac{\partial}{\partial x_i}\left[\overline{\rho}(D+D_t)\frac{\partial M_{n,\beta}}{\partial x_i}\right]+n\overline{\rho}\Omega\left(M_{1,\beta}M_{n-1,\beta}-M_{n,\beta}\right)$$
$$+n\overline{\rho}\int_{-\infty}^{\infty}\psi_\beta^{n-1}S_\beta(\boldsymbol{\psi})f(\boldsymbol{\psi})\mathrm{d}\boldsymbol{\psi},\quad \beta=1,\ldots,N_s,\quad n=0,1,\ldots. \tag{12}$$

The last term on the right-hand side of Equation (12) contains the unknown $f(\boldsymbol{\psi})$ and thus it requires closure. In the QMOM [28–30], the PDF is approximated by a sum of weighted Dirac delta functions:

$$f(\boldsymbol{\psi};\mathbf{x},t) = \sum_{j=1}^{N_q} w_j \prod_{\alpha=1}^{N_s} \delta\left(\psi_\alpha - \psi_{\alpha j}(\mathbf{x},t)\right), \tag{13}$$

where w_j is the weight of the jth Delta function, $\psi_{\alpha j}$ are the abscissas, and N_q is the number of quadrature nodes in the sample space. Using Equation (13), the integral in Equation (12) can be written as

$$\int_{-\infty}^{\infty} \psi_\alpha^{n-1} S_\alpha(\boldsymbol{\psi}) f(\boldsymbol{\psi}) \mathrm{d}\boldsymbol{\psi} = \sum_{j=1}^{N_q} w_j \psi_{\alpha j}^{n-1} S_\alpha\left(\boldsymbol{\psi}_j\right), \quad \alpha = 1,\ldots,N_s, \tag{14}$$

where $\boldsymbol{\psi}_j = (\psi_{1j}, \psi_{2j}, \ldots, \psi_{N_s j})$. Equation (14) means that the closure of chemical source terms is transferred to the calculation of weights w_j and abscissas $\psi_{\alpha j}$. The form of PDF (13) also enables the moments to be expressed in terms of w_j and $\psi_{\alpha j}$:

$$M_{n,\alpha} = \int_{-\infty}^{\infty} \psi_\alpha^n f(\boldsymbol{\psi}) \mathrm{d}\boldsymbol{\psi} = \sum_{j=1}^{N_q} w_j (\psi_{\alpha j})^n. \tag{15}$$

At every point and time, a set of $N_q(1+N_s)$ nonlinear equations (15) are solved for the unknowns w_j and $\psi_{\alpha j}, j = 1,\ldots,N_q, \alpha = 1,\ldots,N_s$, with the same number of moments given from the numerical solution of Equation (12). The solution of Equation (15) is called moment inversion. For the univariate PDF case ($N_s = 1$), the product-difference (PD) [29,40] or Wheeler algorithm [41] can be used to calculate w_j and $\psi_{\alpha j}$ efficiently. Unfortunately, these algorithms cannot be directly extended to the multivariate PDF case. Thus alternative QBMMs, such as DQMOM [28,30] which directly solves the transport equations for weights $w_j(\mathbf{x},t)$ and weighted abscissas $w_j\psi_{\alpha j}(\mathbf{x},t)$, and CQMOM [32,33] which first solves a small nonlinear system of equations with the PD or Wheeler algorithm and then solves multiple linear systems, were developed.

3. Linear quadrature method of moments for univariate PDF

In this section, we propose a new QBMM for the univariate PDF case. In this method, the shape of PDF is no longer presumed. Instead, we assume that the PDF $f(\psi)$ and the source function $S(\psi)$ are smooth so that we can use a conventional quadrature rule to approximate the moment definition and the source integral term as

$$M_n = \int_{\mathbb{R}_\psi} \psi^n f(\psi) \mathrm{d}\psi \approx \sum_{j=1}^{N_L} \omega_j \psi_j^n f_j, \tag{16}$$

$$\int_{\mathbb{R}_\psi} \psi^{n-1} S(\psi) f(\psi) \mathrm{d}\psi \approx \sum_{j=1}^{N_L} \omega_j \psi_j^{n-1} S(\psi_j) f_j, \tag{17}$$

where ψ_j and ω_j are N_L predefined quadrature nodes and weights in the sample space $\mathbb{R}_\psi$, and $f_j = f(\psi_j)$ are the PDF values at the quadrature nodes. For a finite domain $\mathbb{R}_\psi =$

Table 1. Gauss quadrature points and weights in the domain [0,1].

N_L	Quadrature point	Weight
2	(0.2113, 0.7887)	(0.5, 0.5)
3	(0.1127, 0.5, 0.8873)	(0.2778, 0.4444, 0.2778)
4	(0.0694, 0.3300, 0.6700, 0.9306)	(0.1739, 0.3261, 0.3261, 0.1739)
5	(0.0469, 0.2308, 0.5000, 0.7692, 0.9531)	(0.1185, 0.2393, 0.2844, 0.2393, 0.1185)
6	(0.0338, 0.1694, 0.3807, 0.6193, 0.8306, 0.9662)	(0.0857, 0.1804, 0.2340, 0.2340, 0.1804, 0.0857)

$[0, 1]$, ψ_j and ω_j can be Gauss points and weights as shown in Table 1, which is used throughout this paper. We choose Gauss points because the Gauss–Legendre quadrature rule can achieve the highest order of accuracy for a smooth PDF over a finite interval. If the PDF is smooth over the interval $\mathbb{R}_\psi = [a, \infty)$ where a is finite, the Gauss-Laguerre rule may be more preferable. If it is singular at one or two ends, the Gauss-Jacobi rule or Gauss-Chebyshev rule may be more suitable.

We see that the only unknowns in Equation (16) are the PDF values f_j at the preset quadrature nodes. Similar to the moment inversion idea of QMOM, the pointwise values f_j can be solved from the linear system (16) given N_L moments.

Taking the number of quadrature nodes $N_L = 4$ as an example, we can write Equation (16) as the following linear system of equations,

$$\begin{bmatrix} \omega_1 & \omega_2 & \omega_3 & \omega_4 \\ \omega_1\psi_1 & \omega_2\psi_2 & \omega_3\psi_3 & \omega_4\psi_4 \\ \omega_1\psi_1^2 & \omega_2\psi_2^2 & \omega_3\psi_3^2 & \omega_4\psi_4^2 \\ \omega_1\psi_1^3 & \omega_2\psi_2^3 & \omega_3\psi_3^3 & \omega_4\psi_4^3 \end{bmatrix} \begin{bmatrix} f_1 \\ f_2 \\ f_3 \\ f_4 \end{bmatrix} = \begin{bmatrix} M_0 \\ M_1 \\ M_2 \\ M_3 \end{bmatrix}. \tag{18}$$

Generally, the size of this linear system is N_L, thus we need to solve N_L moment transport equations in order to provide $\{M_0, \ldots, M_{N_L-1}\}$ ($M_0 \equiv 1$ need not be solved). The computer time for solving the linear system (18) of size N_L is much smaller than that for solving the nonlinear system (15) of size $2N_q = N_L$ in the QMOM.

We call this new method as Linear Quadrature Method Of Moments (LQMOM) as the moment inversion only involves a linear system. In the followings, we test the PDF reconstruction ability of the LQMOM.

Firstly, the LQMOM is used to reconstruct a Beta distribution PDF given by [42]

$$f(\psi) = \frac{1}{B(\alpha, \beta)} \psi^{\alpha-1}(1-\psi)^{\beta-1}, \quad 0 \le \psi \le 1, \tag{19}$$

where the parameters $\alpha = 2$ and $\beta = 4$, and B is the Beta function. The input moments are exactly defined with (19) as $M_n = \int_0^1 f(\psi)\psi^n \mathrm{d}\psi = \frac{B(\alpha+n,\beta)}{B(\alpha,\beta)}$. The inverted results from the LQMOM and QMOM are shown in Figure 1. It is seen that even the LQMOM with $N_L = 4$ can obtain accurate results. The weights and abscissas inverted by the QMOM with $N_q = 2$ and 3 are plotted as vertical lines (w_j-height, ψ_j-position).

To quantify the concerned quadrature accuracy for the chemical source integral, we use the source function

$$S(\psi) = 21830\psi(1-\psi)\exp(-20/(1+3\psi)) \tag{20}$$

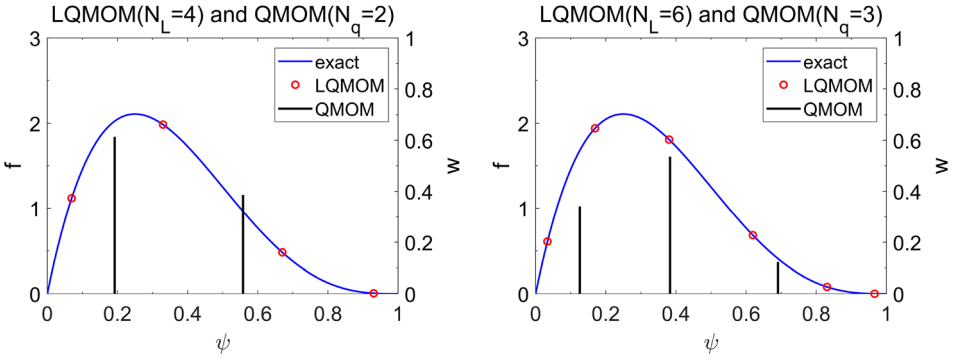

Figure 1. Reconstructed PDF values by the LQMOM (symbols) and weights and abscissas by the QMOM (vertical lines) for the Beta distribution (19) with $\alpha = 2, \beta = 4$ (blue line).

Table 2. Time costs for doing 10^7 times moment inversions for the uni-variate PDF (19) with $\alpha = 2, \beta = 4$.

Method	CPU time (seconds)
QMOM with $N_q = 2$	10.314
QMOM with $N_q = 3$	41.587
LQMOM with $N_L = 4$	0.233
LQMOM with $N_L = 6$	0.482
LQMOM with $N_L = 8$	0.838
LQMOM with $N_L = 20$	6.068

to check the errors of the two QBMMs for the integral $\int_0^1 \psi^{n-1} S(\psi) f(\psi) \mathrm{d}\psi$:

$$\text{error} = \begin{cases} \left| \sum_{j=1}^{N_L} \omega_j \psi_j^{n-1} S(\psi_j) f_j - \int_0^1 \psi^{n-1} S(\psi) f(\psi) \mathrm{d}\psi \right|, & \text{LQMOM}, \\ \left| \sum_{j=1}^{N_q} w_j \psi_j^{n-1} S(\psi_j) - \int_0^1 \psi^{n-1} S(\psi) f(\psi) \mathrm{d}\psi \right|, & \text{QMOM}, \end{cases} \tag{21}$$

where the 'exact' integral can be obtained by a very accurate Gauss integration. The errors of LQMOM with $N_L = 4$ and 6 and QMOM with $N_q = 2$ and 3 for the moment order $n = 3$ are 4.72×10^{-2}, 5.98×10^{-5}, 5.13×10^{-2} and 2.80×10^{-2} in turn, indicating that the LQMOM is more accurate than the QMOM under $N_L = 2N_q$.

Table 2 compares the time costs of QMOM and LQMOM. In the QMOM, the PD algorithm [29,40] is used to compute the elements of the related Jacobi matrix, and the eigenvalue problem of this matrix for obtaining the weights and abscissas is solved using the standard QR algorithm with the iteration tolerance 10^{-14}. It is seen that the LQMOM is several 10 times faster than the QMOM under the same system size $2N_q = N_L$, and LQMOM with $N_L = 20$ is still faster than QMOM with $N_q = 2$.

Secondly, we take $\alpha = 15$ and $\beta = 30$ in the Beta distribution (19) to give a sharper distribution. The results by the LQMOM with $N_L = 6, 12, 16, 20$ and by the QMOM with

$N_q = 2, 3$ are shown in Figure 2. It can be seen that the results by the LQMOM improve with increasing N_L. For $N_L = 6, 12$ there are evidently negative reconstructed PDF values, but for $N_L = 16, 20$ the results get closer to the exact distribution. This implies that the LQMOM cannot reconstruct properly the PDF with a narrow peak distribution. On the other hand, the QMOM with $N_q = 2, 3$ reconstructs normally the weights and abscissas (the bottom in Figure 2). Again, the quadrature errors as defined in (21) for $n = 3$ are 7.35×10^{-2} ($N_L = 6$), 7.60×10^{-7}($N_L = 12$) and 7.06×10^{-8} ($N_L = 20$) for the LQMOM, and 3.42×10^{-3} ($N_q = 2$) and 1.11×10^{-4} ($N_q = 3$) for the QMOM. We see that the LQMOM ($N_L = 12$) has advantage in both accuracy and efficiency over the QMOM ($N_q = 3$).

Thirdly, we compute the beta distribution ($\alpha = 1.5, \beta = 10$) similar to the presumed PDF in chapter 5 of reference [38] used to describe practical non-premixed flame, as see in Figure 3. The recovered PDF values are in fair agreement with the exact solution in spite of having small negative values in the upper side (fully burnt side).

Finally, we admit that the present LQMOM will generate negative and oscillatory PDF values for more extreme distributions such as the sum of two weighted Dirac delta functions. In order to treat more general PDF distributions, we will develop a LQMOM-QMOM hybrid algorithm in Section 4.

4. Hybrid algorithm of LQMOM and QMOM for univariate PDF

4.1. *Detector and LQMOM-QMOM hybrid algorithm*

To build the LQMOM-QMOM hybrid algorithm, a detector to judge whether the unknown PDF distribution is centralized is needed. A natural idea is to use the variance of PDF as the detector. The smaller the variance, the more centralized the distribution is. The variance can be expressed in terms of the first and second moments as

$$\sigma^2 = \int_{\mathbb{R}_\psi} (\psi - M_1)^2 f(\psi) \mathrm{d}\psi = M_2 - M_1^2. \tag{22}$$

It follows that if the PDF is a single Dirac delta function, $f = \delta(\psi - \psi_0)$, then $\sigma = 0$. Thus we can simply set a small threshold like $\epsilon_1 = 0.02$ such that when $\sigma^2 < \epsilon_1$, the PDF distribution is judged as centralized and the QMOM applies, otherwise the LQMOM applies. However, the branch $\sigma^2 \geq \epsilon_1$ can not rule out other extreme cases. For example, for the two-peak distribution $f = 0.4\delta(\psi - 0.3) + 0.6\delta(\psi - 0.9)$, we have $M_1 = 0.66$, $M_2 = 0.522$ and thus $\sigma^2 = M_2 - M_1^2 = 0.084 > \epsilon_1 = 0.02$. But this case cannot be treated by the LQMOM. So we also consider how to detect the case with two-peak PDF distribution. Assuming that the two-peak PDF has the form $f(\psi) = \omega_1\delta(\psi - \psi_1) + \omega_2\delta(\psi - \psi_2)$, we have $M_n = \omega_1\psi_1^n + \omega_2\psi_2^n$, and the moments $M_0(= 1), M_1, M_2, M_3$ should satisfy the following nonlinear system,

$$\begin{cases} M_0 = \omega_1 + \omega_2, \\ M_1 = \omega_1\psi_1 + \omega_2\psi_2, \\ M_2 = \omega_1\psi_1^2 + \omega_2\psi_2^2, \\ M_3 = \omega_1\psi_1^3 + \omega_2\psi_2^3. \end{cases} \tag{23}$$

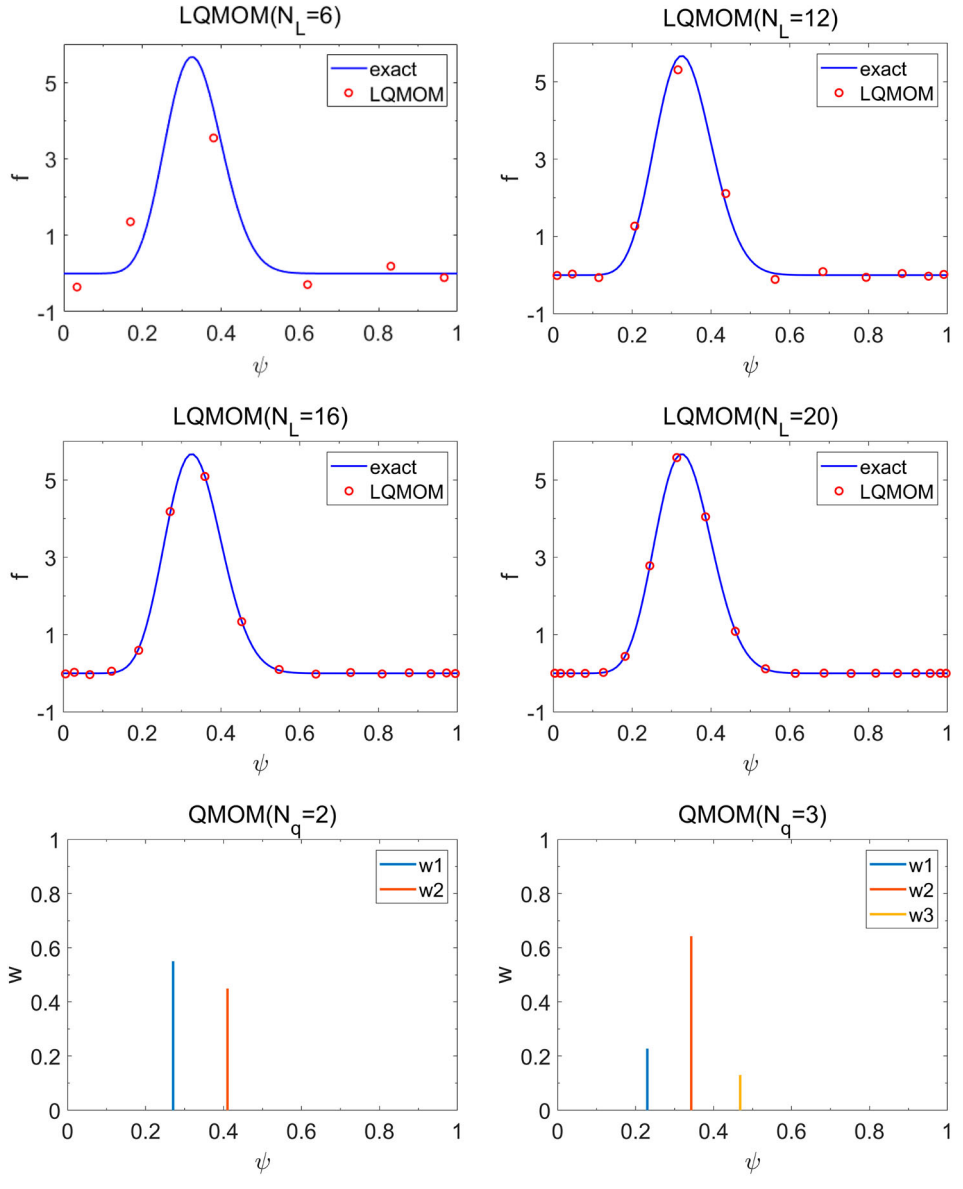

Figure 2. Reconstructed PDF values by the LQMOM with $N_L = 6, 12, 16, 20$ (symbol) for the exact β distribution with $\alpha = 15, \beta = 30$ (curve). The bottom frames show weights and abscissas reconstructed by the QMOM with $N_q = 2$ and 3 (vertical line height for w_j, location for ψ_j).

Here, $\omega_1, \omega_2, \psi_1, \psi_2$ can be uniquely determined by M_0, M_1, M_2, M_3. It can be shown that the higher-order moment $\hat{M}_4$ can be represented in terms of M_0, M_1, M_2, M_3 as

$$\hat{M}_4 = \sum_{j=1}^{2} \omega_j \psi_j^4 = \frac{-M_2^3 + 2M_1 M_2 M_3 - M_0 M_3^2}{M_1^2 - M_0 M_2}. \tag{24}$$

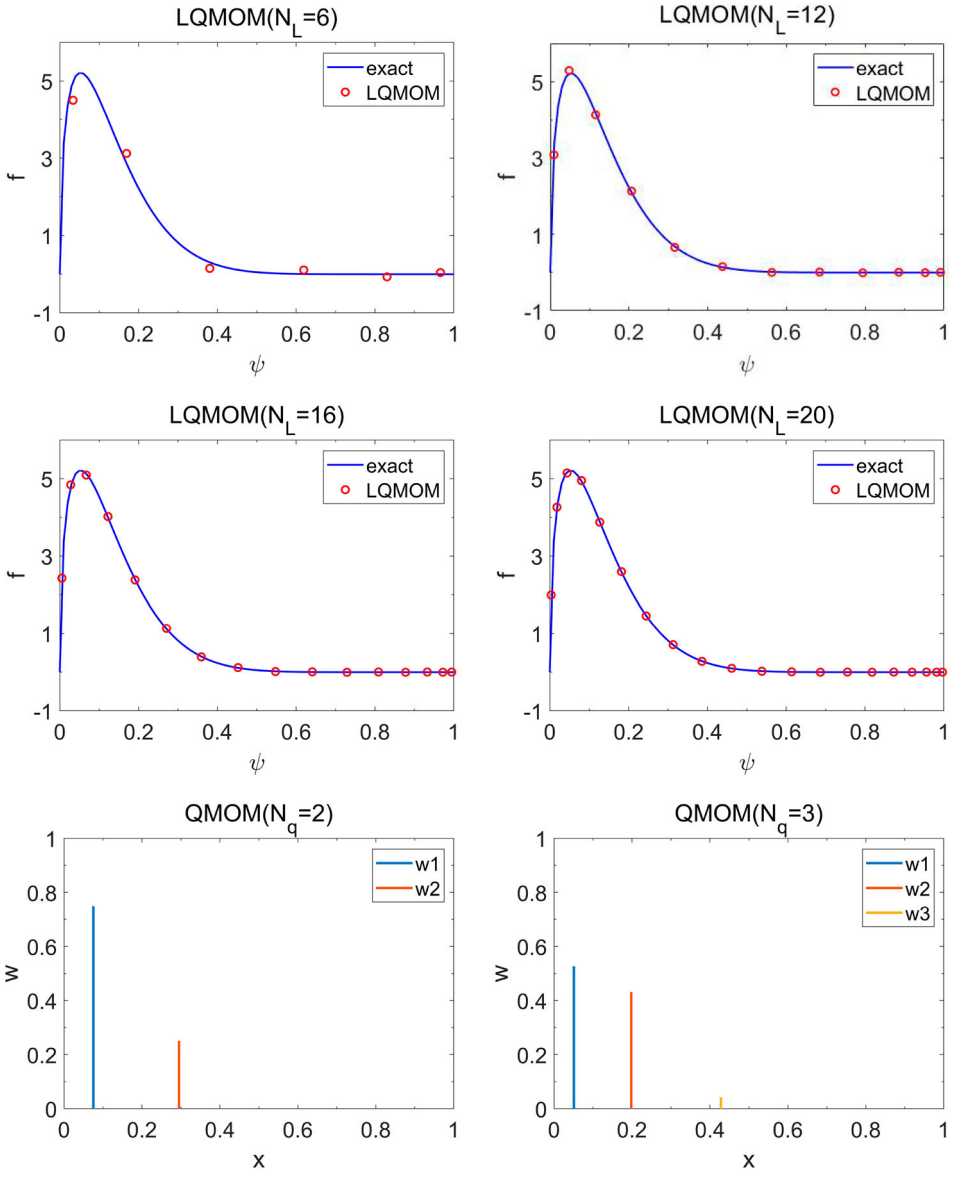

Figure 3. Reconstructed PDF values by the LQMOM with $N_L = 6, 12, 16, 20$ (symbol) for the exact β distribution with $\alpha = 1.5, \beta = 10$ (curve). The bottom frames show weights and abscissas reconstructed by the QMOM with $N_q = 2$ and 3 (vertical line height for w_j, location for ψ_j).

Equation (24) is specific to the two-peak PDF distribution. Thus we can build our hybrid algorithm using the detectors for one-peak and two-peak distributions as follows:

$$\begin{cases} \text{QMOM, if } \left|M_1^2 - M_2\right| < \epsilon_1 \text{ or } \left|M_4 - \dfrac{-M_2^3 + 2M_1M_2M_3 - M_0M_3^2}{M_1^2 - M_0M_2}\right| < \epsilon_2, \\ \text{LQMOM, otherwise,} \end{cases} \tag{25}$$

where $\epsilon_1 = 0.02$ and $\epsilon_2 = 5 \times 10^{-4}$ are empirical threshold values set in default, and $M_0, \ldots, M_4$ are the transported moments. It is hoped that at most times and grid points the PDF distribution is smooth and thus the LQMOM is more frequently used than the QMOM, making the hybrid algorithm gain efficiency over the QMOM alone.

In practice, use of a smaller value of ϵ_1 or ϵ_2 will allocate more work to the LQMOM. If the LQMOM still reconstructs negative PDF values, we go back to use the QMOM to ensure the realizability. In fact, peak distributions only occur in the boundary (such as incoming streams) and initial conditions. After a short time of transition, a large portion of the flow domain can be calculated by the LQMOM.

In the following, a one-dimensional moment transport equation example is used to demonstrate the performance of the LQMOM-QMOM hybrid algorithm.

4.2. *Testing LQMOM-QMOM in plug-flow reactor with imperfect mixing*

A simple one-dimensional reaction benchmark [43,44] is used to check the performance of the hybrid algorithm. It describes the evolution of a reaction progress variable $\phi(x,t)$ in the domain $x \in [0,1]$ ($\phi = 0$ means unburnt gas and $\phi = 1$ burnt gas). A scalar $\psi \in [0,1]$ corresponding to $\phi(x,t)$ is the internal coordinate of the PDF. For simplicity, we assume that the density and velocity are constant, $\rho(x,t) = v(x,t) \equiv 1$. The boundary conditions are $f(\psi;0,t) = \delta(\psi)$ at the inlet boundary and $\frac{\partial^2 f}{\partial \psi^2}(\psi;1,t) = 0$ at the outlet boundary. The initial condition is $f(\psi;x,0) = \delta(\psi - 1)$. The moment transport equation (cf. Equation (12)) is given by

$$\frac{\partial M_n}{\partial t} + \frac{\partial M_n}{\partial x} = \frac{\partial}{\partial x}\left(D\frac{\partial M_n}{\partial x}\right) + n\Omega(M_1 M_{n-1} - M_n) + n\int_0^1 \psi^{n-1} S(\psi) f(\psi) \mathrm{d}\psi, \quad (26)$$

where $D = 0.1$ is the total diffusion coefficient and $\Omega = 10$ the mixing frequency. Two different formulas for the chemical source term as used in [44] are considered here.

First, we consider a linear source term as given by

$$S(\psi) = a_1(1 - \psi), \quad (27)$$

where $a_1 = 3$. Assuming $\frac{\partial M_n}{\partial t} = 0$, we can get the exact solution of the first-order moment equation (26) with the source term (27) as follows,

$$M_1 = 1 - \exp(-bx), \quad \text{where} \quad b = \frac{1}{2}\{\sqrt{1 + 4a_1 D} - 1\}/D.$$

In the numerical solution of Equation (26) with the source (27), we use the WENO-Z5 finite difference scheme [45] for the convective term and the third-order TVD-Runge Kutta method [46,47] for time marching. A second-order central scheme is used for the diffusion term, and the source terms and mixing terms are treated explicitly.

We use 101 grid points and a time step $\Delta t = 2.5 \times 10^{-4}$, and the end time is $T = 2$ which can guarantee that the steady state is reached. We compare the QMOM ($N_q = 2$) and the hybrid LQMOM ($N_L = 4$)-QMOM($N_q = 2$) algorithm. The computed mean $\bar{\phi} = M_1$ and standard variance σ are shown in Figure 4. It can be seen that the M_1 results by the two methods are in good agreement with the exact solution, and the σ results between the two methods are nearly same. Figure 5 shows the M_1 profiles at four different times computed with the hybrid algorithm. We can see that at the initial time the hybrid algorithm

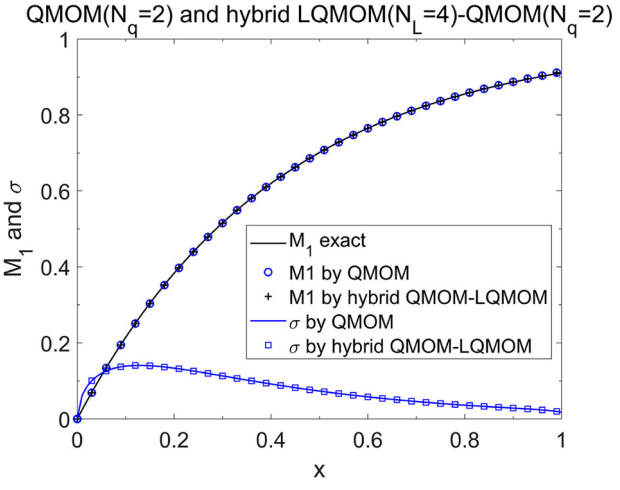

Figure 4. Comparison for the first-order moment M_1 and standard variance σ among the QMOM, hybrid algorithm, and exact solution for the plug-flow reactor problem with the linear source (27) at time $T = 2$.

uses QMOM at every grid point due to the initial peak distribution. As the time goes on, the hybrid algorithm uses LQMOM at more and more grid points except near the inlet and the remanent initial state regions. The total computational time of the hybrid algorithm is 65.44% that of the QMOM alone.

Second, we consider a more stiff exponential reaction source term (20) for Equation (26). To solve this case, we adopt the Strang splitting method [48] with two flow steps and one reaction step in between, i.e.

$$M_n(t + \Delta t) = L_f\left(\frac{\Delta t}{2}\right) L_r(\Delta t) L_f\left(\frac{\Delta t}{2}\right) M_n(t),$$

where L_f is the convection-diffusion-mixing operator and L_r the chemical reaction operator. L_f is solved with the same schemes as in the linear source case, and L_r is marched with the forward Euler scheme with 10 sub-steps. We take 41 grid points, a time step $\Delta t = 2.5 \times 10^{-4}$, and a larger threshold $\epsilon_1 = 0.05$ for Equation (25) for more use of the QMOM in the hybrid algorithm. We tested various hybridizations of $N_q = 2, 3$ with $N_L = 4, 6, 8, 10, 12, 14, 16$ to see the influence of different numbers of quadrature points on the numerical results. It is found that the difference between $N_q = 2$ and $N_q = 3$ with same N_L is small, but that between different N_L with same N_q is large when $N_L \leq 8$. So we finally choose the LQMOM ($N_L = 14$)-QMOM ($N_q = 3$) hybrid algorithm. The computed first-order moment at $t = 0.5$ and $t = 1.5$, and standard variance at $t = 1$ are shown in Figure 6. We see that the hybrid algorithm and the single QMOM ($N_q = 3$) can produce results close to the reference solution computed with the single QMOM on 201 grid points.

Figure 7 shows the first-order moment profiles at different times. We see that the spatial domain calculated by the LQMOM is smaller than that in the linear source case (Figure 5). Nevertheless, the total computational time of the hybrid algorithm is still 68.75% that of the stand-alone QMOM.

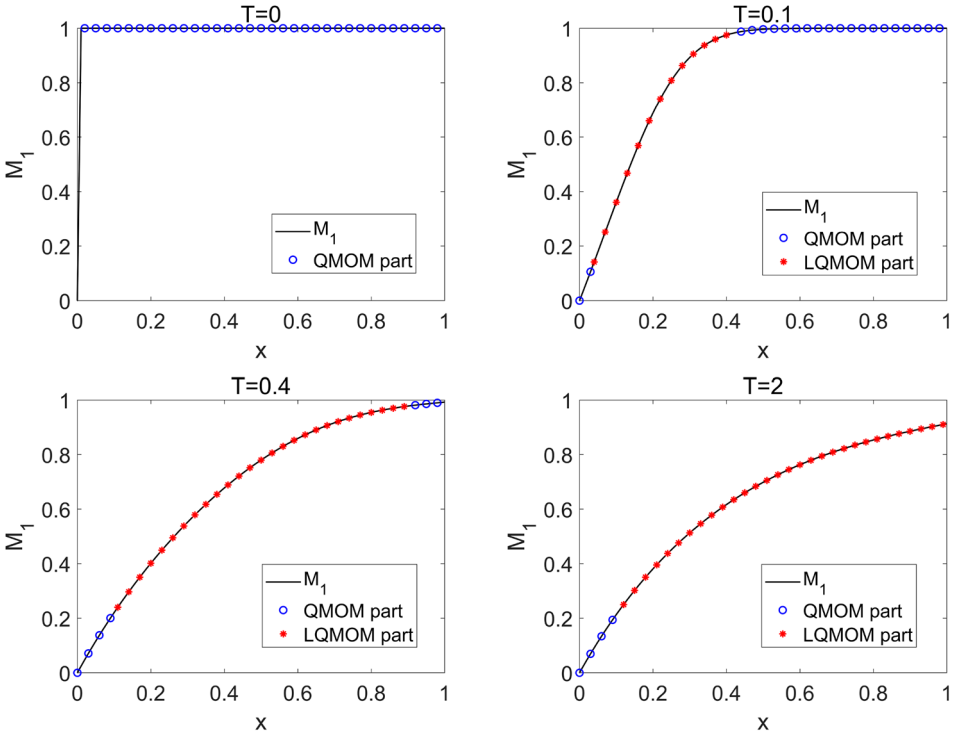

Figure 5. Profiles of the first-order moment M_1 at different times calculated by the LQMOM-QMOM hybrid algorithm for the plug-flow reactor with the linear source (27). Blue and red dots indicate points at which the QMOM and LQMOM are used, respectively.

5. Extension of LQMOM and hybrid algorithm to multivariate PDF

Like the QMOM, the LQMOM can not be directly applied to the multivariate PDF case. Fortunately, the QMOM has already been extended to multivariate PDF as the Conditional Quadrature Method Of Moments (CQMOM) [32]. In this section, we extend the LQMOM to multivariate PDF by referring to the basic idea of CQMOM.

For ease of description, we take the bivariate PDF case as an example. Extension to multivariate PDF cases will be described later. Let the two internal coordinates of PDF be the mixture fraction ξ and reaction progress variable Y, where $0 \leq (\xi, Y) \leq 1$. The joint scalar ξ-Y PDF transport equation is given as [35]:

$$\frac{\partial F}{\partial t} + \frac{\partial\left(\tilde{u}_i F\right)}{\partial x_i} = \frac{\partial}{\partial x_i}\left[\overline{\rho}(D + D_t)\frac{\partial\left(F/\overline{\rho}\right)}{\partial x_i}\right] + \frac{\partial}{\partial \xi}\left[\Omega(\xi - \tilde{\xi})F\right] - \frac{\partial}{\partial Y}\left[S(\xi, Y)F\right]. \quad (28)$$

Denote M_{nm} as the mixed moments of the PDF $\tilde{f} = F/\overline{\rho}$, where n and m represents the order of moments. The mixed moments are defined as:

$$M_{nm} = \int_{\mathbb{R}_Y}\int_{\mathbb{R}_\xi} \xi^n Y^m \tilde{f}(\xi, Y)\mathrm{d}\xi\,\mathrm{d}Y, \quad n, m = 0, 1, \ldots. \quad (29)$$

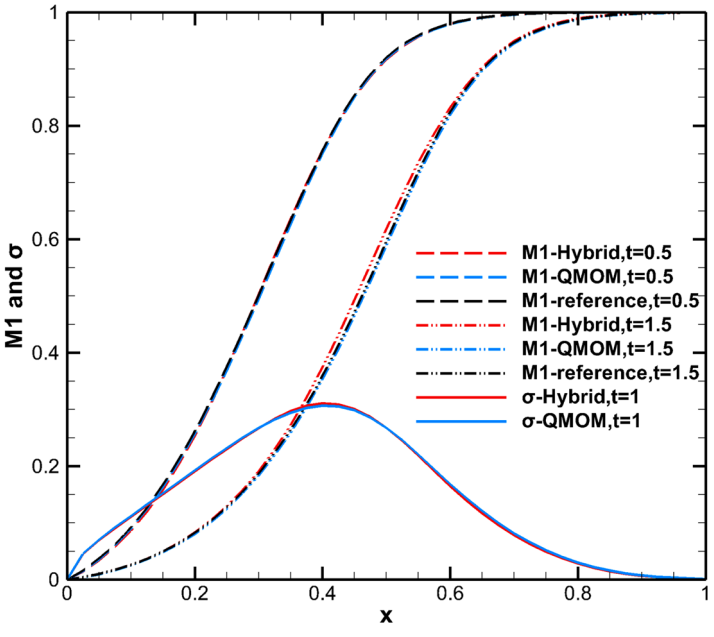

Figure 6. Comparison of the first-order moment M_1 and standard variance among the hybrid algorithm, QMOM and reference solution for plug-flow reactor with the exponential source (20). The reference solution is obtained with the stand-alone QMOM ($N_q = 3$) on 201 grid points.

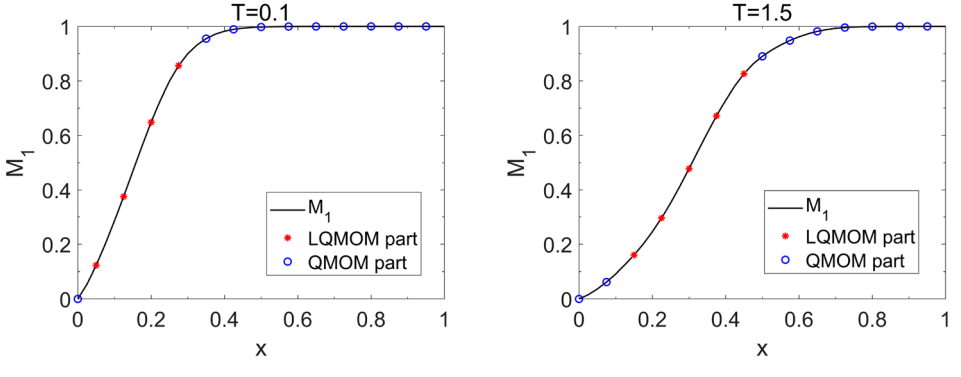

Figure 7. M_1 profiles at different times computed by the LQMOM-QMOM hybrid algorithm for the plug-flow reactor with the exponential source case (20). Blue and red dots indicate spatial positions where the QMOM and LQMOM are used, respectively.

From now on, we suppress the integration domain for brevity. The moment transport equations can be derived via integration of Equation (28) in the ξ-Y space and are given as

$$\frac{\partial\,(\overline{\rho}M_{nm})}{\partial t}+\frac{\partial\,(\overline{\rho}\tilde{u}_i M_{nm})}{\partial x_i}=\frac{\partial}{\partial x_i}\left[\overline{\rho}(D+D_t)\frac{\partial M_{nm}}{\partial x_i}\right]+n\overline{\rho}\Omega\,(M_{10}M_{n-1m}-M_{nm})$$
$$+\,m\overline{\rho}\iint\xi^n Y^{m-1}S(\xi,Y)\tilde{f}(\xi,Y)\mathrm{d}\xi\,\mathrm{d}Y. \tag{30}$$

The CQMOM [32] can be used to close the integral term as briefly reviewed below.

5.1. *CQMOM*

Take ξ as the primary internal coordinate. Define $f(Y|\xi)$ as the conditional density function of Y conditioned at ξ. The bivariate PDF $\tilde{f}$ can be expressed equivalently as

$$\tilde{f}(\xi, Y) = f(\xi) f(Y|\xi). \tag{31}$$

As per the classical QMOM, each of the two density functions in the right-hand side of Equation (31) can be approximated by the sum of weighted Dirac delta functions, thus

$$\tilde{f}(\xi, Y) = \sum_{\alpha=1}^{N_1} w_\alpha \delta(\xi - \xi_\alpha) \sum_{\beta=1}^{N_2} w_{\alpha,\beta} \delta(Y - Y_{\alpha,\beta}). \tag{32}$$

Here, N_1 and N_2 are the numbers of quadrature nodes in the ξ (primary) and Y (secondary) directions, w_α and ξ_α are the primary weights and abscissas, and $w_{\alpha,\beta}$ and $Y_{\alpha,\beta}$ are the secondary ones. All the weights and abscissas are unknowns.

Using Equations (31) and (32), the mixed moments (29) can be expressed as

$$\begin{aligned} M_{nm} &= \int f(\xi) \xi^n \left(\int f(Y|\xi) Y^m \mathrm{d}Y \right) \mathrm{d}\xi \\ &= \sum_{\alpha=1}^{N_1} \sum_{\beta=1}^{N_2} w_\alpha w_{\alpha,\beta} \xi_\alpha^n Y_{\alpha,\beta}^m. \end{aligned} \tag{33}$$

And the chemical source term in the moment equations (30) can be closed as

$$R_{nm} = m\overline{\rho} \int \xi^n Y^{m-1} S(\xi, Y) \tilde{f}(\xi, Y) \mathrm{d}\xi \mathrm{d}Y = m\overline{\rho} \sum_{\alpha=1}^{N_1} \sum_{\beta=1}^{N_2} w_\alpha w_{\alpha,\beta} \xi_\alpha^n Y_{\alpha,\beta}^{m-1} S(\xi_\alpha, Y_{\alpha,\beta}). \tag{34}$$

It is evident from Equation (32) that the number of unknowns is $2(N_1 + N_1 N_2)$. If a K-variate PDF in the conditional form $\tilde{f}(\boldsymbol{\psi}) = f(\psi_1) f(\psi_2|\psi_1) \cdots f(\psi_K|\psi_1, \ldots, \psi_{K-1})$ is approximated with the Dirac delta functions, the number of unknowns is $2(N_1 + N_1 N_2 + \cdots + N_1 N_2 \cdots N_K)$, which is very large. Therefore, to reduce computational cost the CQMOM always uses $N_2 = \cdots = N_K = 1$, thus $w_{\alpha,\beta} = w_{\alpha,\beta,\gamma} = \cdots = 1$, and the total number of unknowns becomes $2N_1 + (K-1)N_1 = N_1 + N_1 K$. For the bivariate case, we take $N_1 = 2$ as an example while $N_2 = 1$. Now Equation (32) becomes

$$\tilde{f}(\xi, Y) = \sum_{\alpha=1}^{2} w_\alpha \delta(\xi - \xi_\alpha) \delta(Y - Y_\alpha), \tag{35}$$

which has six unknowns. If we select a set of six low order mixed moments as

$$\begin{cases} M_{00} \\ M_{10} \\ M_{20} \\ M_{30} \end{cases}, \quad \begin{cases} M_{01} \\ M_{11} \end{cases}, \tag{36}$$

we have the following nonlinear equations from Equation (33),

$$\begin{cases} w_1 + w_2 = M_{00} \\ w_1\xi_1 + w_2\xi_2 = M_{10} \\ w_1\xi_1^2 + w_2\xi_2^2 = M_{20} \\ w_1\xi_1^3 + w_2\xi_2^3 = M_{30} \end{cases}, \quad \begin{cases} w_1 Y_1 + w_2 Y_2 = M_{01} \\ w_1\xi_1 Y_1 + w_2\xi_2 Y_2 = M_{11} \end{cases}. \tag{37}$$

The basic idea of CQMOM is to solve the left nonlinear equations in (37) by the PD or Wheeler algorithm to obtain $\{w_1, w_2, \xi_1, \xi_2\}$ at first, and then take the results into the right equations so that they become linear equations. $\{Y_1, Y_2\}$ are solved out as

$$\begin{cases} Y_1 = \dfrac{1}{w_1(\xi_2 - \xi_1)} \left(\xi_2 M_{01} - M_{11}\right), \\ Y_2 = \dfrac{1}{w_2(\xi_2 - \xi_1)} \left(-\xi_1 M_{01} - M_{11}\right). \end{cases} \tag{38}$$

Finally, the chemical source term (34) can be calculated as

$$R_{nm} = m\overline{\rho} \sum_{\alpha=1}^{N_1} w_\alpha \xi_\alpha^n Y_\alpha^{m-1} S(\xi_\alpha, Y_\alpha). \tag{39}$$

The above CQMOM can be easily extended to N_s scalar joint PDF cases. Now Equation (35) is replaced by $\tilde{f}(\psi_1, \ldots, \psi_{N_s}) = \sum_{j=1}^{N_1} w_j \delta(\psi_1 - \phi_{1j}) \prod_{\beta=2}^{N_s} \delta(\psi_\beta - \phi_{\beta j})$. So we need to solve $N_1 + N_1 N_s$ mixed moment transport equations (actually less one because $M_{0\ldots0} \equiv 1$). If we properly choose a scalar as the primary coordinate ψ_1, and adopt a set of mixed moments similar to the form (36),

$$\begin{cases} M_{\mathbf{00}} \\ M_{\mathbf{10}} \\ \vdots \\ M_{(2N_1-1)\mathbf{0}} \end{cases}, \begin{cases} M_{0\mathbf{1}0} \\ M_{1\mathbf{1}0} \\ \vdots \\ M_{(N_1-1)\mathbf{1}0} \end{cases}, \ldots, \begin{cases} M_{0\mathbf{0}1} \\ M_{1\mathbf{0}1} \\ \vdots \\ M_{(N_1-1)\mathbf{0}1} \end{cases}, \tag{40}$$

we can build a series of systems like Equation (37). To solve these systems, we first solve a nonlinear system of $2N_1$ equations built upon the first moment vector in Equation (40) for the primary weights $\{w_j\}_{j=1}^{N_1}$ and abscissas $\{\phi_{1j}\}_{j=1}^{N_1}$ by using the PD or Wheeler algorithm. With these results, we then solve $N_s - 1$ linear systems of N_1 equations for the subsidiary abscissas $\{\phi_{\beta j}\}_{j=1}^{N_1}, \beta = 2, \ldots, N_s$ built upon the remaining moment vectors in Equation (40), where the βth moment vector is composed of $\{M_{k_1 k_2 \ldots k_\beta \ldots k_{N_s}}\}_{k_1=0}^{N_1-1}$ with $k_2 = \cdots = k_{N_s} = 0$ except that $k_\beta = 1$.

5.2. *LCQMOM* (*linear CQMOM*)

To extend the LQMOM to the multivariate PDF case, we refer to the conditional PDF idea of the CQMOM [32,33]. We rewrite the bivariate PDF here as

$$\tilde{f}(\xi, Y) = f(\xi) f(Y|\xi).$$

Here, the univariate PDF $f(\xi)$ remains continuous and will be treated by the LQMOM while the conditional PDF is approximated as $f(Y|\xi) = \sum_{\beta=1}^{N_2} \omega_{\xi,\beta}\delta(Y - Y_{\xi,\beta})$. To reduce computational cost as said in Section 5.1 we use $N_2 = 1$ and thus $\omega_{\xi,\beta} = 1$.

The mixed moments can be approximated as follows:

$$\begin{aligned} M_{nm} &= \int \xi^n f(\xi) \left(\int Y^m f(Y|\xi) \mathrm{d}Y \right) \mathrm{d}\xi \\ &\approx \sum_{\alpha=1}^{N_1} \left[f(\xi_\alpha) \xi_\alpha^n \omega_\alpha \int Y^m f(Y|\xi_\alpha) \mathrm{d}Y \right] \\ &= \sum_{\alpha=1}^{N_1} \omega_\alpha \xi_\alpha^n f(\xi_\alpha) Y_\alpha^m, \end{aligned} \tag{41}$$

where ξ_α and ω_α are the preset quadrature nodes and weights, and $f(\xi_\alpha)$ and Y_α are the unknowns. Once they are solved out, the chemical source term can be closed as

$$\begin{aligned} R_{nm} &= m\overline{\rho} \int \xi^n Y^{m-1} S(\xi, Y) \tilde{f}(\xi, Y) \mathrm{d}\xi \mathrm{d}Y \\ &= m\overline{\rho} \int \xi^n f(\xi) \left(\int Y^{m-1} S(\xi, Y) f(Y|\xi) \mathrm{d}Y \right) \mathrm{d}\xi \\ &\approx m\overline{\rho} \sum_{\alpha=1}^{N_1} \omega_\alpha \xi_\alpha^n f(\xi_\alpha) Y_\alpha^{m-1} S(\xi_\alpha, Y_\alpha). \end{aligned} \tag{42}$$

In order to show how to solve for $(f(\xi_\alpha), Y_\alpha), \alpha = 1, \ldots, N_1$ from Equation (41), we take $N_1 = 4$ as an example. The number of unknowns is $2N_1 = 8$. We choose a set of eight low order mixed moments as follows,

$$\begin{cases} M_{00} \\ M_{10} \\ M_{20} \\ M_{30} \end{cases}, \quad \begin{cases} M_{01} \\ M_{11} \\ M_{21} \\ M_{31} \end{cases}. \tag{43}$$

Given the two moment vectors, we can establish two systems of equations as:

$$\begin{cases} \sum_{\alpha=1}^{N_1} \omega_\alpha f_\alpha = M_{00}, \\ \sum_{\alpha=1}^{N_1} \omega_\alpha \xi_\alpha f_\alpha = M_{10}, \\ \sum_{\alpha=1}^{N_1} \omega_\alpha \xi_\alpha^2 f_\alpha = M_{20}, \\ \sum_{\alpha=1}^{N_1} \omega_\alpha \xi_\alpha^3 f_\alpha = M_{30}. \end{cases}, \quad \begin{cases} \sum_{\alpha=1}^{N_1} \omega_\alpha f_\alpha Y_\alpha = M_{01}, \\ \sum_{\alpha=1}^{N_1} \omega_\alpha \xi_\alpha f_\alpha Y_\alpha = M_{11}, \\ \sum_{\alpha=1}^{N_1} \omega_\alpha \xi_\alpha^2 f_\alpha Y_\alpha = M_{21}, \\ \sum_{\alpha=1}^{N_1} \omega_\alpha \xi_\alpha^3 f_\alpha Y_\alpha = M_{31}. \end{cases} \tag{44}$$

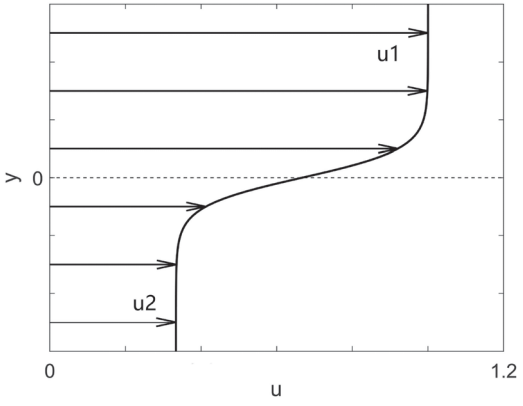

Figure 8. Sketch of initial velocity profile of the 2D shear layer flow.

We first solve for $f_\alpha, \alpha = 1, 2, \ldots, N_1$ from the left linear system by using the LQMOM. Substituting the solved results to the right system in Equation (44), we can obtain a linear system, and then we solve it for $Y_\alpha, \alpha = 1, 2, \ldots, N_1$. Finally, the solved values of f_α and Y_α are taken into the source integral term (42) for closure.

To extend the above procedure to a N_s-variate PDF, we preset N_1 quadrature nodes and weights in a properly chosen primary internal coordinate direction ψ_1. The PDF is approximated as $\tilde{f}(\psi_1, \ldots, \psi_{N_s}) = f(\psi_1) \prod_{\beta=2}^{N_s} \delta(\psi_\beta - \phi_\beta|\psi_1)$. In order to establish N_s linear systems of size N_1, we select $N_1 N_s$ mixed moments similar to the set (43), i.e. the first moment vector is $\{M_{k_1\mathbf{0}}, k_1 = 0, \ldots, N_1 - 1\}$, involving only the primary direction, while the βth moment vector for $\beta = 2, \ldots, N_s$ is $\{M_{k_1\mathbf{0}k_\beta\mathbf{0}}, k_1 = 0, \ldots, N_1 - 1, k_\beta = 1\}$, involving both the primary direction and the subsidiary βth direction. The number of moment transport equations to solve is $N_1 N_s$ (actually less one because $M_{\mathbf{0}} \equiv 1$). We call this method as Linear Conditional Quadrature Method Of Moments (LCQMOM). Although this method has lower computational cost in the moment inversion stage, it may be more time consuming than the CQMOM because it needs a larger N_1 and thus more moment transport equations need to be solved.

To reduce the computational cost of LCQMOM, we make an assumption that the N_1 conditional PDFs conditioned at the primary nodes can be reduced to two. Take $N_1 = 4$ as an example. For the preset quadrature nodes $\xi_1 < \xi_2 < \xi_3 < \xi_4$ in the primary direction, two Dirac delta functions can be assumed as:

$$f(Y|\xi_1) = f(Y|\xi_2) = \delta(Y - \hat{Y}_1), \quad f(Y|\xi_3) = f(Y|\xi_4) = \delta(Y - \hat{Y}_2). \tag{45}$$

Then, only the first two equations associated with M_{01} and M_{11} in the right system in Equation (44) are needed:

$$\begin{cases} M_{01} = (\omega_1 f_1 + \omega_2 f_2)\, \hat{Y}_1 + (\omega_3 f_3 + \omega_4 f_4)\, \hat{Y}_2, \\ M_{11} = (\omega_1 \xi_1 f_1 + \omega_2 \xi_2 f_2)\, \hat{Y}_1 + (\omega_3 \xi_3 f_3 + \omega_4 \xi_4 f_4)\, \hat{Y}_2. \end{cases} \tag{46}$$

This is a linear system and is solved for $(\hat{Y}_1, \hat{Y}_2)$, and then we use $Y_1 = Y_2 = \hat{Y}_1$, $Y_3 = Y_4 = \hat{Y}_2$ in evaluating the chemical source terms (42). We call this simplified method as LCQMOM-S. Compared with the LCQMOM, the LCQMOM-S can (i) reduce the number

of moment transport equations from $N_1 N_s$ to $N_1 + 2(N_s - 1)$, and (ii) reduce the size of the $N_s - 1$ linear systems from N_1 to 2.

For robustness reason as said in the end of Section 3, we use the hybrid LCQMOM(-S) and CQMOM algorithm for multivariate PDFs according to the switch function (25) with (M_1, M_2, M_3, M_4) replaced by $(M_{10}, M_{20}, M_{30}, M_{40})$.

6. Numerical results

Two- and three-dimensional benchmark problems are used to test the performance of the present LCQMOM(-S)-CQMOM hybrid algorithm used in the LES/PDF method for turbulent combustion. The spatial and temporal schemes for the LES equations (the first three equations in Equation (3)) are same as introduced in Section 4.2. Further, the WENO-Z5 scheme [45] is implemented in the characteristic fields and the global Lax-Fridriches flux splitting [49] is used. The moment transport Equations (30) and (12) are treated with the Strang splitting method as described in Section 4.2. The exception is the enthalpy source term, Equation (10), which is not stiff and is treated explicitly together with the convection–diffusion-mixing operator. For the discretization of Equation (10), the forward Euler scheme is applied to $\partial p/\partial t$, the second-order MUSCL-TVD scheme [50] to $\tilde{u}_i \partial \overline{p}/\partial x_i$, and the second-order central scheme to the viscous dissipation term.

6.1. *Two-dimensional compressible reactive shear flow*

The spatially developing shear layer flow includes two parallel flows with different velocities. The flow field can form a complex vortex structures and avoid the influence of wall boundary layer. Therefore, it is a benchmark problem in turbulence research [51,52]. As shown in Figure 8, u_1 and u_2 are the velocities of the upper and lower infinities of the shear flow, and generally one takes $u_1 = 1$ and $u_2 = 1/3$. The initial mean velocity profile and thermodynamic variables can be constructed by the hyperbolic tangent function as follows [53,54],

$$\begin{aligned} u &= (1 + R\tanh(2y))/(1 + R), \\ v &= 0, \\ p &= \frac{1}{\gamma \mathrm{Ma}^2}, \\ T &= 1 + \frac{1}{2}\sqrt{\mathrm{Pr}}(\gamma - 1)\mathrm{Ma}^2(1 - u)(1 - u_2), \end{aligned} \tag{47}$$

where the velocity ratio parameter ($u_1 = 1$ is as the reference velocity) is

$$R = \frac{1 - u_2}{1 + u_2}.$$

We take $\mathrm{Re} = 600, \mathrm{Ma} = 0.8, \gamma = 1.4, \mathrm{Pr} = 0.75$. The computational domain is $[0, 150] \times [-20, 20]$. By adding random disturbances with the amplitude of $0.2u(y)$ to the velocity components u and v on the left boundary, the shear instability can be promoted to form complex vortex structures. In this example, the LES equations (the first three equations in Equation (3)) are assumed to be decoupled from the species mass equations as done in [18,35], therefore the flow variables $(\overline{\rho}, \tilde{u}, \tilde{v}, \tilde{T})$ can be obtained by solving the LES

equations for a single-species ideal gas. A uniform 300×80 Cartesian grid is used, CFL $=$ 0.5, and the Smagorinsky model parameter $C_S = 0.14$.

In order to test the QBMMs in the reactive shear flow, the moment transport equation (30) of the bivariate PDF for the mixture fraction $Z = \xi \in [0, 1]$ and reaction progress variable $Y \in [0, 1]$, are solved with the quantities $(\overline{\rho}, \tilde{u}, \tilde{v}, D, D_t)$ provided from the decoupled numerical solution of the LES equations. The initial values of Z and Y are given as follows:

$$\begin{cases} Z = 0.5\,(\tanh(2y) + 1.0)\,, \\ Y = 0. \end{cases} \tag{48}$$

A simple reaction source term [35,52] for Equation (30) is given as

$$S(Z, Y) = K\left(\frac{Z}{Z_{st}} - Y\right)\left(\frac{1 - Z}{1 - Z_{st}} - Y\right), \tag{49}$$

where the reaction rate coefficient $K = 0.1$ and the stoichiometric mixture fraction $Z_{st} =$ 0.5. In the CQMOM and LCQMOM(-S), the mixture fraction Z is chosen as the primary internal coordinate, and the CQMOM takes the number of nodes $N_1 = 2$ while the LQMOM(-S) takes $N_1^{\mathrm{L}} = 4$. The switch function (25) for the LCQMOM(-S)-CQMOM algorithm uses the parameters $\epsilon_1 = 0.02$ and $\epsilon_2 = 5 \times 10^{-4}$ (ϵ_2 is not used since M_4 is not solved due to $N_1^{\mathrm{L}} = 4$).

As a comparison to the QBMMs, the 'LES scalar' method as in [35] is used here, which solves the LES equations with the three scalar transport equation (50) for the filtered mixture fraction $\tilde{Z}$, second moment $\widetilde{Z^2}$, and reaction progress variable $\tilde{Y}$ respectively. $\widetilde{Z^2}$ is used to compute the variance $\widetilde{Z''^2}$ for comparison with the variance $\sigma^2 = M_{20} - (M_{10})^2$ calculated via Equation (22). The three scalar transport equations are

$$\begin{aligned}
\frac{\partial\left(\overline{\rho}\tilde{Z}\right)}{\partial t} + \frac{\partial\left(\overline{\rho}\tilde{u}_i\tilde{Z}\right)}{\partial x_i} &= \frac{\partial}{\partial x_i}\left[\rho(D + D_t)\frac{\partial\tilde{Z}}{\partial x_i}\right], \\
\frac{\partial\left(\overline{\rho}\widetilde{Z^2}\right)}{\partial t} + \frac{\partial\left(\overline{\rho}\tilde{u}_i\widetilde{Z^2}\right)}{\partial x_i} &= \frac{\partial}{\partial x_i}\left[\rho(D + D_t)\frac{\partial\widetilde{Z^2}}{\partial x_i}\right] - \overline{\rho}\tilde{\chi}, \\
\frac{\partial\left(\overline{\rho}\tilde{Y}\right)}{\partial t} + \frac{\partial\left(\overline{\rho}\tilde{u}_i\tilde{Y}\right)}{\partial x_i} &= \frac{\partial}{\partial x_i}\left[\rho(D + D_t)\frac{\partial\tilde{Y}}{\partial x_i}\right] + S(\tilde{Z}, \tilde{Y}),
\end{aligned} \tag{50}$$

where the sub-filter fluctuation of the reaction source term S is neglected as in [35]. To keep consistency with the mixing frequency $\Omega = C_\phi \frac{D+D_t}{\Delta^2}$ in the moment transport equation (30), the scalar dissipation rate of the second moment, $\tilde{\chi}$, is taken as

$$\tilde{\chi} = C_\phi \frac{D + D_t}{\Delta^2}\widetilde{Z''^2}, \quad \text{where } \widetilde{Z''^2} = \widetilde{Z^2} - (\tilde{Z})^2. \tag{51}$$

And

$$D = \frac{\mu}{\overline{\rho}\mathrm{Sc}}, \quad D_t = \frac{\mu_t}{\overline{\rho}\mathrm{Sc}_t}, \quad \mathrm{Sc} = \mathrm{Sc}_t = 1.0, \quad C_\phi = 2. \tag{52}$$

Figure 9 compares the contours of the filtered reaction progress variable $\tilde{Y}$ at the non-dimensional time $t = 400$ computed by the four methods: LES scalar, CQMOM,

Table 3. Computer times for marching 1000 steps for the 2D reactive shear layer flow.

Method	Time (s)
LES scalar	173.962
CQMOM ($N_1 = 2$)	513.329
LCQMOM($N_1^{\mathrm{L}} = 4$)-CQMOM ($N_1 = 2$)	577.333
LCQMOM-S ($N_1^{\mathrm{L}} = 4$)-CQMOM ($N_1 = 2$)	407.141

LCQMOM-CQMOM, and LCQMOM-S-CQMOM. All these methods use one-way coupling, i.e. the LES part provide information to the scalar/PDF part but not vice versa. We see that the formation of shear vortices begins around $x = 50$ and the reaction happens mostly in vortex centres. The LES scalar method predicts an earlier chemical reaction (larger $\tilde{Y}$), while the CQMOM, LCQMOM-CQMOM, and LCQMOM-S-CQMOM results are close, particularly between CQMOM and LCQMOM-S-CQMOM. Notice that the LES scalar result looks like Figure 2 in [35].

Since the shear vortices have moved outside the right boundary for $t > 400$, we conducted time-averaged statistics from $t = 800$ to the final time $t_{\mathrm{end}} = 2000$ for the four sections $x = 20, 30, 50, 100$. Figure 10 compares sectional profiles of the time-averaged variables $\tilde{Y}, \tilde{Z}$ and $\widetilde{Z''^2}$ computed by the four methods. It is seen that the $\tilde{Y}$ result by the LES scalar method is the largest. The $\tilde{Y}$ result by LCQMOM-CQMOM is between LES scalar and CQMOM. Interestingly, the result by LCQMOM-S-CQMOM is more close to CQMOM than LCQMOM-CQMOM. The reason may be that both the LCQMOM-S and CQMOM ($N_1 = 2$) use two Dirac delta functions to approximate the conditional PDF but the LCQMOM uses four ($N_1^{\mathrm{L}} = 4$). The $\tilde{Z}$ and $\widetilde{Z''^2}$ results in the right frame in Figure 10 between the four methods are close to each other, and are comparable to Figure 3 in [35]. However, as the computational parameters used are different from those in [35], the numerical results have difference, and thus we do not plot their results in this figure.

Lastly, we compare computational costs of the four methods in Table 3. The LES scalar method is the fastest, which solves the three scalar transport equation (50). The LCQMOM-S-CQMOM hybrid algorithm is the second fastest, which solves six moment transport equations as the CQMOM ($N_1^{\mathrm{L}} + 2(N_s - 1) = 6 = N_1 + N_1 N_s$), and the size of $N_s - 1$ linear systems is only 2. However, the computer time is reduced by 20% compared to the CQMOM, this is due to two reasons: (1) the cost for the moment inversion is small compared with that for solving the moment transport equations; (2) the fraction of computational domain calculated by LCQMOM-S is small. This is clearly seen in Figure 11. The LCQMOM-CQMOM is the slowest, mainly due to solving $N_1^{\mathrm{L}} N_s = 8$ moment transport equations, two more than that in the CQMOM. Although the moment inversion of LQMOM can reduce the time cost partially, it is not enough to offset the increased time cost for solving the two more moment transport equations.

6.2. *Three-dimensional high-speed reacting air/H_2 jet*

We consider the reacting air/H_2 jet problem in LAERTE experimental data (see [55] and references therein), which has been simulated by Karaca et al. [56]. The physical parameters used are given in Table 4. The computational domain is $250 \times 30 \times 30\,\mathrm{mm}^3$ from the round nozzle exit plane ($x = 0$) to the downstream plane ($x = 250$) and encompassing

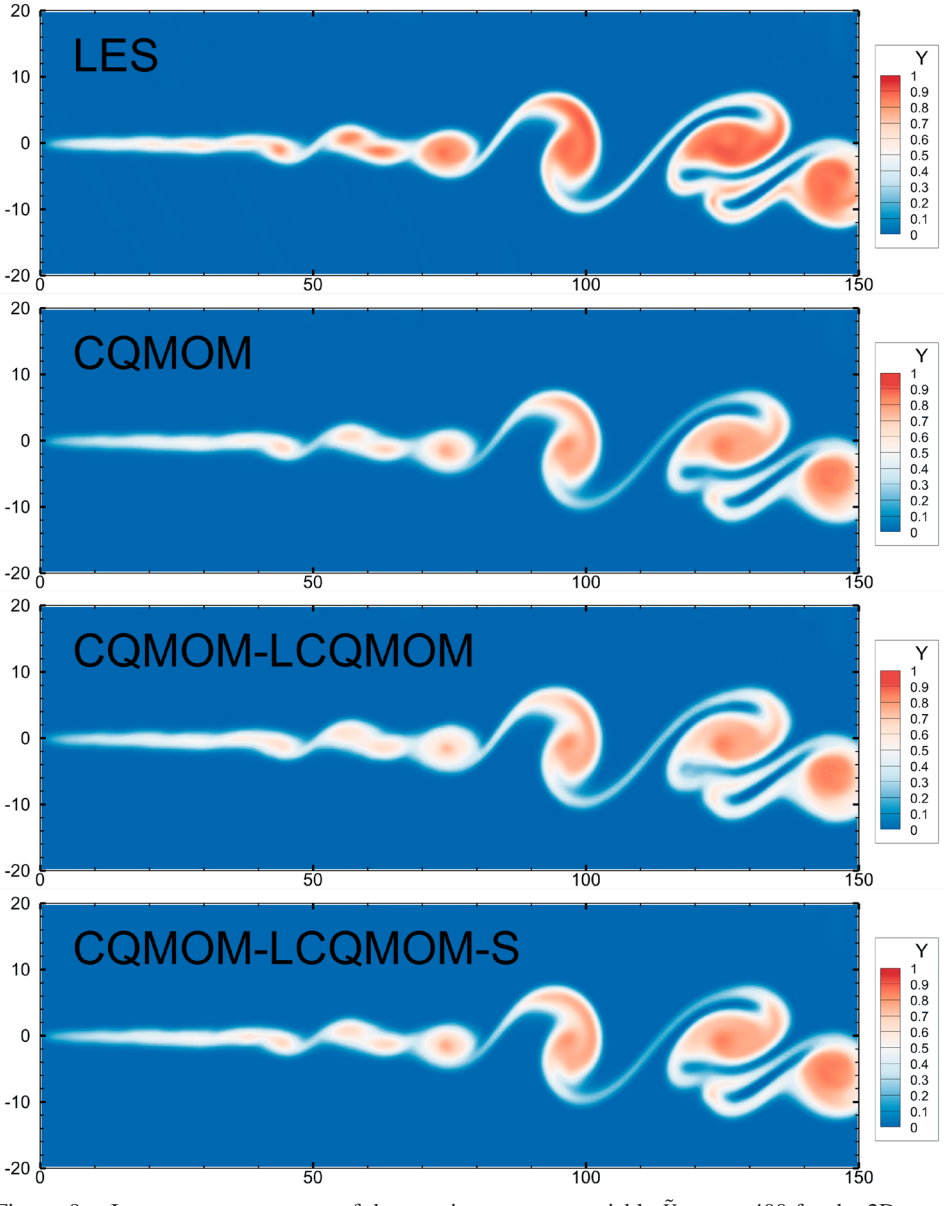

Figure 9. Instantaneous contours of the reaction progress variable $\tilde{Y}$ at $t = 400$ for the 2D reactive shear layer flow computed on the 300×80 grid using four methods: LES scalar, CQMOM, LCQMOM-CQMOM and LCQMOM-S-CQMOM.

the jet centreline $(x, 0, 0)$. The computational domain and the inflow velocity profile $u(y)$ on the jet centreline section $z = 0$ are illustrated in Figure 12(a,b). The C++ function `rand` generated random numbers are multiplied with 7.5% $u(y)$ and added to the velocity $(\tilde{u}, \tilde{v}, \tilde{w})$ on the inlet plane. The chemical reaction mechanism with 9 species and 19 reactions [57] are adopted. It takes about 0.2 ms for the jet to flow from the nozzle exit to the

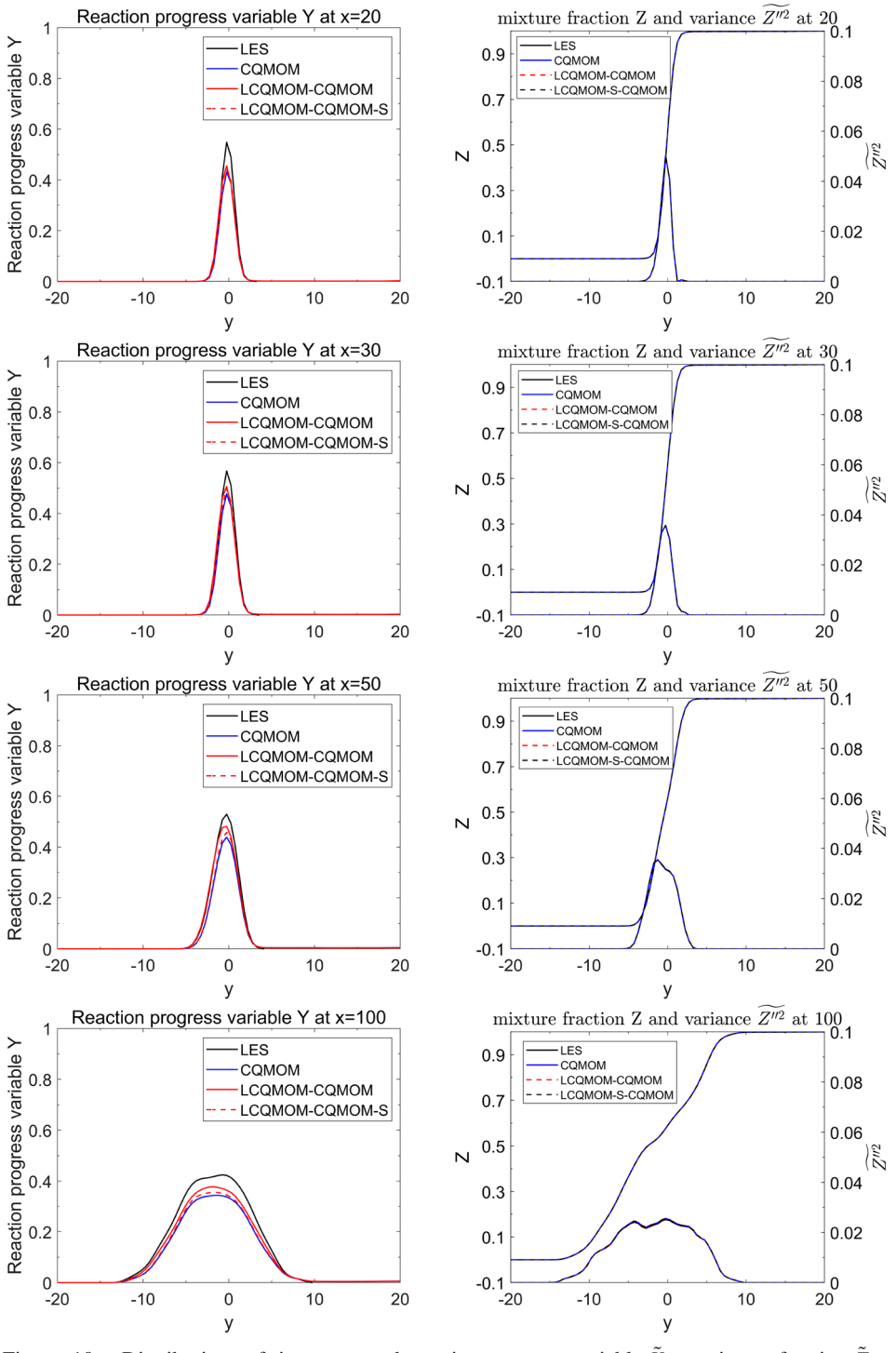

Figure 10. Distributions of time averaged reaction progress variable $\tilde{Y}_{\text{ave}}$, mixture fraction $\tilde{Z}_{\text{ave}}$ and variance $\widetilde{Z''^2_{\text{ave}}}$ along the y direction at $x = 20, 30, 50, 100$ stations for the 2D reactive shear layer flow.

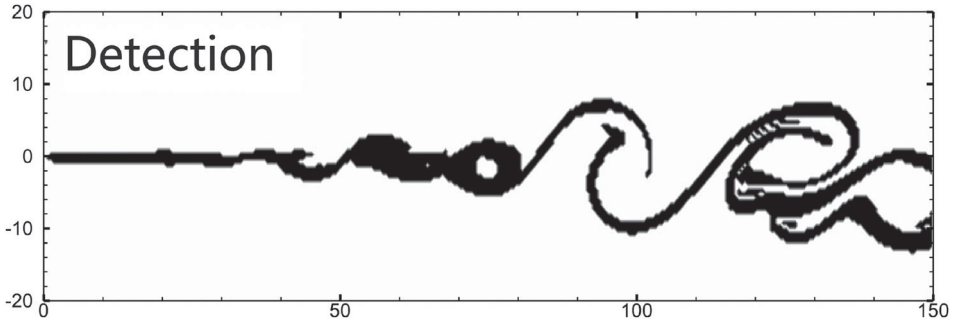

Figure 11. The detection result at $t = 400$ by the detector (25) in the LCQMOM-S-CQMOM hybrid algorithm for the 2D reactive shear layer flow. The dark region marks where the LCQMOM-S is applied.

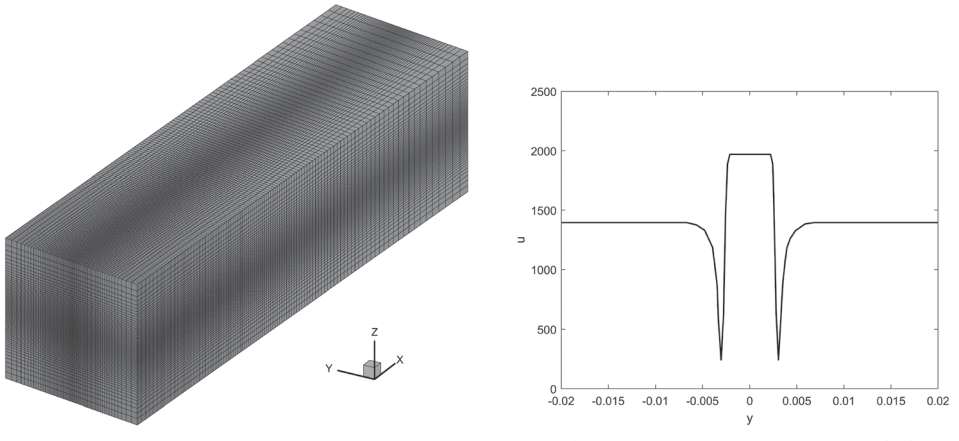

(a) Perspective of the computational domain.

(b) Inlet velocity profile taken from [56].

Figure 12. Computational domain and inlet velocity profile for reacting air/H_2 LAERTE jet problem [55]. (a) Perspective of the computational domain and (b) Inlet velocity profile taken from [56].

Table 4. LAERTE experimental conditions [55].

	H_2 jet	Air co-flow
U (m/s)	1970	1366
T (K)	160	1170
P (kPa)	84	92
μ (kg m^{-1}s^{-1})	0.729×10^{-5}	4.604×10^{-5}
ρ (kg m^{-3})	0.127	0.259

downstream boundary. Therefore, we conduct time average statistics from time $t = 0.2$ ms to the simulation end time $t_{\text{end}} = 0.4$ ms.

The numerical simulation uses $256(x) \times 64(y) \times 64(z)$ Cartesian grid points. The grid is clustered to the nozzle centreline and the inlet plane (see Figure 12(a)) and CFL number is set to 0.5. The governing equations are transformed in generalized curvilinear coordinates

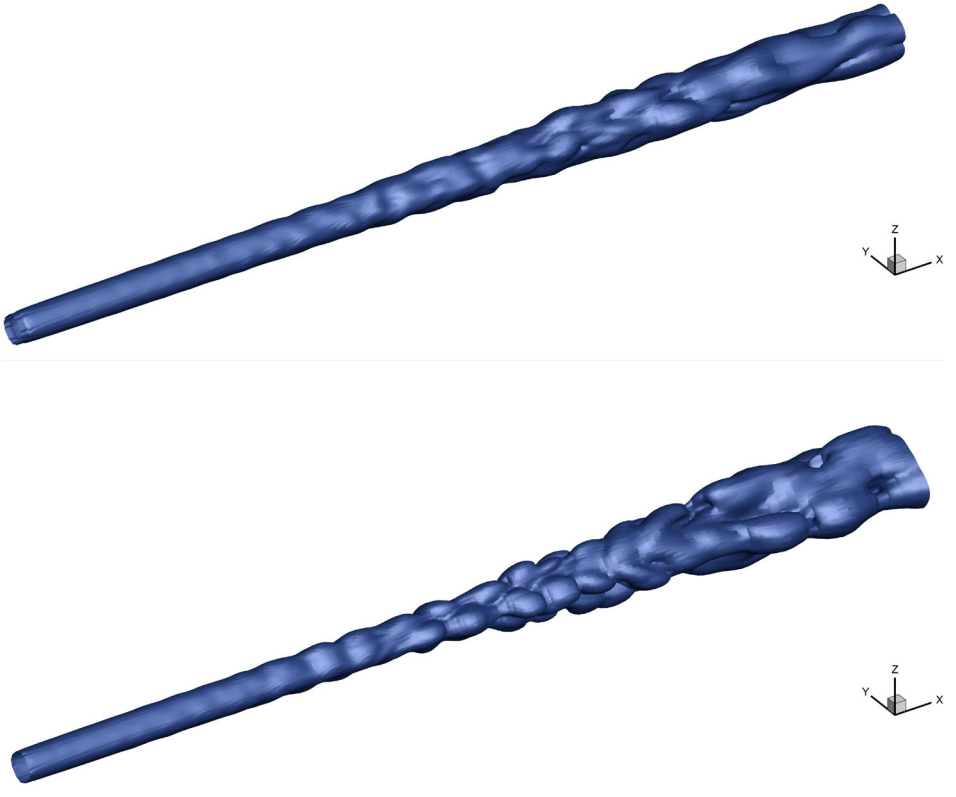

Figure 13. Reacting air/H_2 LAERTE jet. Instantaneous iso-surfaces of the mixture fraction $Z_{st} = 0.0297$ at $t_{end} = 0.4$ ms computed on the $256 \times 64 \times 64$ grid with (a) LES alone, (b) LCQMOM-S-CQMOM.

and discretized with the numerical schemes mentioned in the beginning of Section 6. The Smagorinsky model parameter $C_S = 0.1$ is used for this problem.

The number of quadrature nodes for the CQMOM is taken as $N_1 = 2$, and that for the LCQMOM(-S) is taken as $N_1^{\mathrm{L}} = 4$. The mass fraction of hydrogen is selected as the primary internal coordinate ψ_1. The scalar joint PDF contains the mixture enthalpy and eight chemical species excluding nitrogen ($N_s = 9$).

As a comparison, the LES alone method is also used for this problem. It solves the full Equation (3) including the total energy and species mass conservation equations. The chemical reaction source terms are implicitly modelled by substituting the Favre filtered variables directly into the Arrhenius law to compute $\tilde{\dot{\omega}}_\alpha$.

To compare the computational costs of the four methods, we count the number of transport equations which need to be solved. The LES alone method solves the mass, momentum, total energy and species equations, totalling $5 + (N_s - 1) = 13$ equations. The LES/CQMOM ($N_1 = 2$) solves the mass and momentum equations but the energy and mass fractions are calculated using the moment transport equations, totalling $4 + N_1 + N_1 N_s - 1 = 4 + 2 + 2 \times 9 - 1 = 23$ (less one due to $M_{\mathbf{0}} \equiv 1$) equations. The LES/LCQMOM ($N_1^{\mathrm{L}} = 4$) solves $4 + N_1^{\mathrm{L}} N_s - 1 = 4 + 4 \times 9 - 1 = 39$ equations, and the LES/LCQMOM-S ($N_1^{\mathrm{L}} = 4$) solves $4 + N_1^{\mathrm{L}} + 2(N_s - 1) - 1 = 23$ equations. It can be seen that the latter three methods need to solve more transport equations than the first

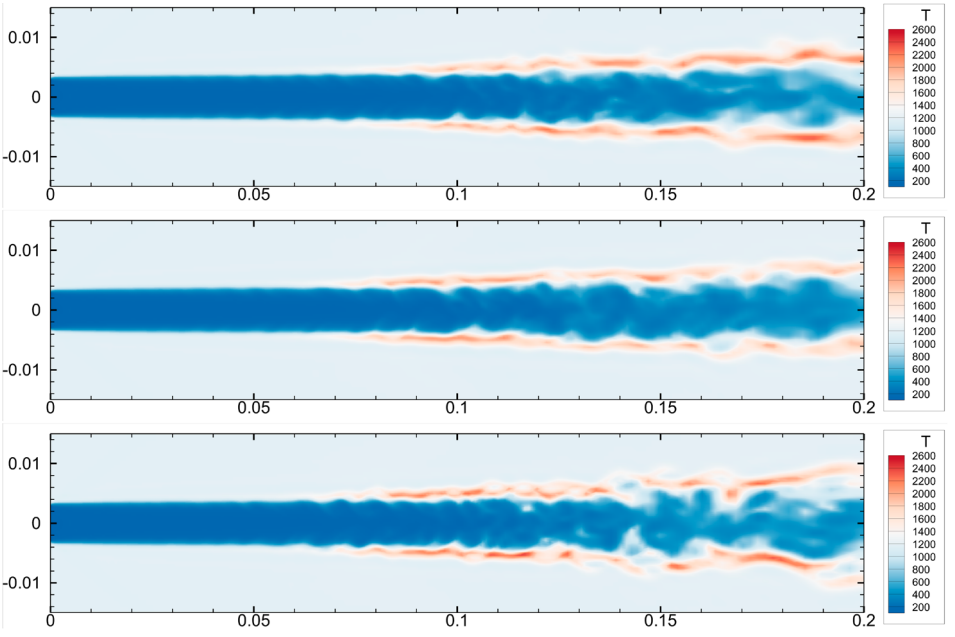

Figure 14. Time-averaged temperature contours in the $z = 0$ plane at $t_{\text{end}} = 0.4$ ms for reacting air/H_2 LAERTE jet on the $256 \times 64 \times 64$ grid with the LES alone (top), CQMOM (middle), and LCQMOM-S-CQMOM (bottom).

method, however, they can yield similar results as the LES alone with coarser grids. Notice that the LCQMOM-S has a much lower inversion cost than the CQMOM even if both have the same number of moment transport equations.

We follow [56] to look at the mixture fraction defined by $Z = (sY_{\text{H}_2} - Y_{\text{O}_2} + Y_{\text{O}_2}^{\infty})/(sY_{\text{H}_2}^{\infty} + Y_{\text{O}_2}^{\infty})$, where $s = W_{\text{O}_2}/(2W_{\text{H}_2})$ is the mass stoichiometric ratio, and W_{H_2} and W_{O_2} are the molecular weights. The stoichiometric mixture fraction $Z_{\text{st}} = 1/(sY_{\text{H}_2}^{\infty}/Y_{\text{O}_2}^{\infty} + 1)$ results from the condition $Y_{\text{H}_2} = Y_{\text{O}_2} = 0$. In this problem, $Y_{\text{H}_2}^{\infty} = 1$ in the hydrogen jet and $Y_{\text{O}_2}^{\infty} = 0.2447$ in the air co-flow [56], so $Z_{\text{st}} = 0.0297$. Figure 13 shows the perspective view of the instantaneous Z_{st} iso-surface at $t_{\text{end}} = 0.4$ ms. It is seen that the LCQMOM-S-CQMOM has clearer vortical structures in the upstream zone than the LES alone due to later reactions. The results by the CQMOM and LCQMOM-QMOM are similar to the LCQMOM-S-CQMOM and thus are not shown.

Figure 14 shows time-averaged temperature contours in the $z = 0$ centreline plane at $t_{\text{end}} = 0.4$ ms computed with the three methods: LES alone, CQMOM and LCQMOM-S-CQMOM. It is seen that high temperature zones due to exothermic chemical reactions appear on surfaces of the jet. Unlike instantaneous contours, the time-averaged temperature contours by the various methods are more similar to each other.

The inconsistency issue of a LES/PDF hybrid method is a concern. in the present work, the temperature is a redundant variable because it can be computed from either $f_1(T, e_{\text{les}}, \mathbf{Y}_{\text{pdf}}) = 0$ or $f_2(T, h_{\text{pdf}}, \mathbf{Y}_{\text{pdf}}) = 0$, where e, h and $\mathbf{Y}$ are the mixture internal energy, enthalpy, and species mass fractions with the subscripts labelling the LES or PDF side. The relative inconsistent error of temperature is defined as $|T_{\text{M}}/T_{\text{les}} - 1|$, where T_{les} is calculated from the $f_1 = 0$ relation and T_{M} from the $f_2 = 0$ relation. Figure 15 shows

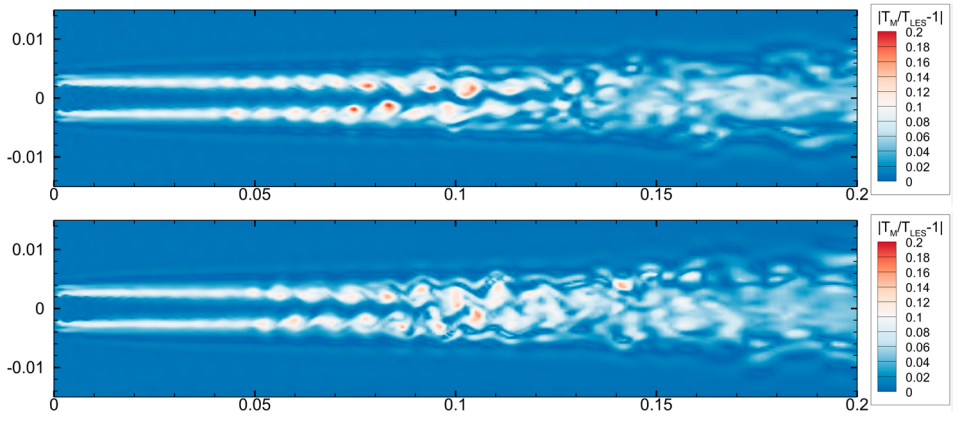

Figure 15. Contours of the temperature inconsistency error averaged over $t \in [0.2, 0.4]$ ms in the $z = 0$ plane for reacting air/H_2 LAERTE jet on the $256 \times 64 \times 64$ grid with the CQMOM (up) and LCQMOM-S-CQMOM (down).

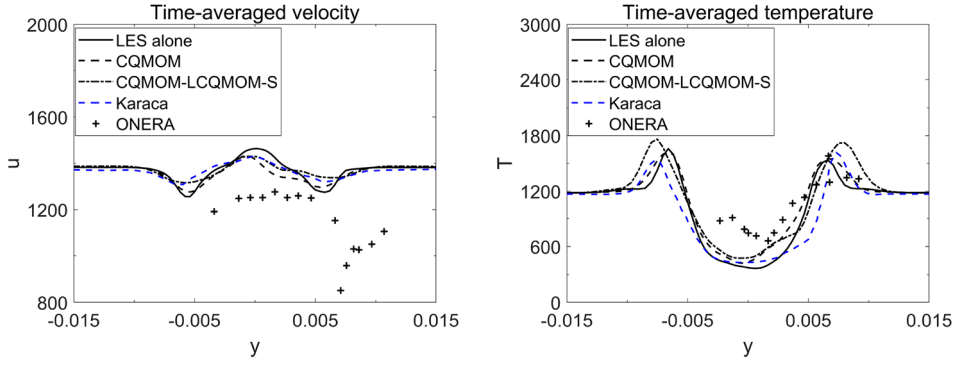

Figure 16. Reacting air/H_2 LAERTE jet. Time-averaged velocity (left) and temperature (right) profiles on the line $(x, z) = (0.21, 0)$ computed by three different methods on the $256 \times 64 \times 64$ grid compared with Karaca's numerical [56] and ONERA's experimental [55] results. The Smagorinsky model parameter $C_S = 0.1$.

contours of the inconsistent errors of CQMOM and LCQMOM-S-CQMOM. It can be seen that the two methods have similar results, with the maximum error 20% initializing at $x \approx 0.1$ and dropping down to 10% at $x \approx 0.2$. How to reduce the inconsistent error will be our future task.

Figure 16 shows distributions of the time-averaged axial velocity component u and temperature T in the spanwise line $(x, z) = (0.21, 0)$. It can be seen that the results with LES alone, CQMOM, and LCQMOM-S-CQMOM are comparable to the numerical result in Figure 23 by Karaca et al. [56], but differ much from the experimental result by ONERA group [55]. On the whole, the temperature peaks and their locations computed by CQMOM and LCQMOM-S-CQMOM are more comparable to Karaca et al. [56] than the LES alone.

Finally, to give the flame lifting height, we first conduct time average of the temperature field in the interval $t \in [0.2, 0.4]$ ms, and then we find the position of $T = 1220$ K (50 K higher than the temperature of co-flow) in the time-averaged temperature contours and take its most right front as the flame lifting height. We compare the numerical result with the

Table 5. Flame lifting height in the air/H_2 reacting jet flow.

Method	Height (cm)
LES alone	5.589
CQMOM ($N_1 = 2$)	8.089
LCQMOM-S ($N_1^L = 4$)-CQMOM ($N_1 = 2$)	10.281
ONERA's LAERTE experimental result	17

experimental data [55] in Table 5. It can be seen that results of the flame lifting height calculated with CQMOM and CQMOM-LCQMOM-S are closer to the experimental results than the LES alone. The slightly better agreement between the LCQMOM-S-CQMOM result and the experiment one compared to the CQMOM may be due to that more quadrature nodes ($N_1^L = 4$) are used in the primary direction than the CQMOM with two nodes ($N_1 = 2$), thus enhancing accuracy.

7. Conclusion

The linear quadrature method of moments (LQMOM) for the univariate PDF case and its extension to the multivariate PDF case are presented. The LQMOM assumes that the PDF distribution is smooth and uses a set of preset quadrature nodes and weights for approximating the moment definition. In this way, a linear equation system is established for the PDF values at the quadrature nodes, and the inversion cost is much less than the nonlinear moment inversion in the QMOM. However, the LQMOM does not work well for non-smooth PDF distributions, and thus we use the LQMOM-QMOM hybrid algorithm for the time being. Numerical tests show that the hybrid algorithm is still more efficient than the QMOM. The LQMOM is extended to the multivariate PDF case by referring to the main idea of the conditional quadrature method of moments (CQMOM). To reduce the computational cost of the resultant LCQMOM, we develop the simplified version, LCQMOM-S. Finally, the LCQMOM-S-CQMOM hybrid algorithm is applied to two- and three-dimensional turbulent reactive flows. The numerical results show that this hybrid algorithm can produce comparable results and reduce the overall time by about 20% compared with the CQMOM.

The major shortcoming of LQMOM or LCQMOM is that it is prone to generate negative PDF values for non-smooth PDF distributions. In the follow-up work, we shall study how to erase this deficiency. Finally, how to reduce the inconsistency error of the LES/PDF hybrid method and how to select the primary internal coordinate for the LCQMOM and CQMOM are worthy of further study.

Disclosure statement

No potential conflict of interest was reported by the author(s).

Funding

This work is supported by National Natural Science Foundation of China [Grant Nos. 12071470, 12161141017]. The computations are carried out on high performance computers of the State Key Laboratory of Scientific and Engineering Computing (LSEC), Chinese Academy of Sciences.

References

[1] J.B. Staubach, *Multidisciplinary design optimization, MDO, the next frontier of CAD/CAE in the design of aircraft propulsion systems*, Tech. Rep., AIAA/ICAS International Air and Space Symposium and Exposition: The Next 100 Year, 2003

[2] F.T. Johnson, E.N. Tinoco, and N.J. Yu, *Thirty years of development and application of CFD at Boeing commercial airplanes, Seattle*, Comput. Fluids 34 (2005), pp. 1115–1151.

[3] A. Abbas-Bayoumi and K. Becker, *An industrial view on numerical simulation for aircraft aerodynamic design*, J. Math. Ind. 1 (2011), pp. 1–14.

[4] J. Janicka and A. Sadiki, *Large eddy simulation of turbulent combustion systems*, Proc. Combust. Inst. 30 (2005), pp. 537–547.

[5] H. Pitsch, *Large-eddy simulation of turbulent combustion*, Annu. Rev. Fluid Mech. 38 (2006), pp. 453–482.

[6] N. Peters, *Laminar diffusion flamelet models in non-premixed turbulent combustion*, Prog. Energy Combust. Sci. 10 (1984), pp. 319–339.

[7] S.B. Pope, *PDF methods for turbulent reactive flows*, Prog. Energy Combust. Sci. 11 (1985), pp. 119–192.

[8] S.B. Pope, *Computations of turbulent combustion: Progress and challenges*, Proc. Combust. Inst. 23 (1991), pp. 591–612.

[9] F.A. Jaberi, P.J. Colucci, S. James, P. Givi, and S.B. Pope, *Filtered mass density function for large-eddy simulation of turbulent reacting flows*, J. Fluid Mech. 401 (1999), pp. 85–121.

[10] P. Givi, *Filtered density function for subgrid scale modeling of turbulent combustion*, AIAA J. 44 (2006), pp. 16–23.

[11] A.Y. Klimenko and R.W. Bilger, *Conditional moment closure for turbulent combustion*, Prog. Energy Combust. Sci. 25 (1999), pp. 595–687.

[12] W.K. Bushe and H. Steiner, *Conditional moment closure for large eddy simulation of nonpremixed turbulent reacting flows*, Phys. Fluids 11 (1999), pp. 1896–1906.

[13] P.A. McMurtry, S. Menon, and A.R. Kersteinet, *Linear eddy modeling of turbulent combustion*, Engery Fuels 7 (1993), pp. 817–826.

[14] S. Menon and W.H. Calhoon, *Subgrid mixing and molecular transport modeling in a reacting shear layer*, Symp. Combust. 26 (1996), pp. 59–66.

[15] T.D. Butler and P. O'Rourke, *A numerical method for two-dimensional unsteady reacting flows*, Proc. Combust. Inst. 16 (1976), pp. 1503–1515.

[16] O. Colin, F. Ducros, D. Veynante, and T. Poinsot, *A thickened flame model for large eddy simulations of turbulent premixed combustion*, Phys. Fluids 12 (2000), pp. 1843–1863.

[17] G. Wang, M. Boileau, and D. Veynante, *Implementation of a dynamic thickened flame model for large eddy simulations of turbulent premixed combustion*, Combust. Flame 158 (2011), pp. 2199–2213.

[18] P. Givi, *Model-free simulations of turbulent reactive flows*, Prog. Energy Combust. Sci. 15 (1989), pp. 1–107.

[19] S.B. Pope, *Turbulent Flows*, Cambridge University Press, Cambridge, UK, 2000.

[20] V. Raman and H. Pitsch, *A consistent LES/filtered-density function formulation for the simulation of turbulent flames with detailed chemistry*, Proc. Combust. Inst. 31 (2007), pp. 1711–1719.

[21] A. Hsu, Y.L. Tsai, and M. Raju, *Probability density function approach for compressible turbulent reacting flows*, AIAA J. 32 (1994), pp. 1407–1415.

[22] V. Raman, R.O. Fox, and A.D. Harvey, *Hybrid finite-volume/transported PDF simulations of a partially premixed methane-air flame*, Combust. Flame 136 (2004), pp. 327–350.

[23] T. Hasret, S.B. Pope, and M. Metin, *A LES/PDF simulator on block-structured meshes*, Combust. Theory Model. 23 (2019), pp. 1–41.

[24] L. Valiño, *A field Monte Carlo formulation for calculating the probability density function of a single scalar in a turbulent flow*, Flow Turbul. Combust. 60 (1998), pp. 157–172.

[25] W. Jones and V. Prasad, *Large eddy simulation of the Sandia flame series (D–F) using the Eulerian stochastic field method*, Combust. Flame 157 (2010), pp. 1621–1636.

[26] C. Gong, M. Jangi, X.S. Bai, J.H. Liang, and M.B. Sun, *Large eddy simulation of hydrogen combustion in supersonic flows using an Eulerian stochastic fields method*, Int. J. Hydrog. Energy 42 (2017), pp. 1264–1275.

[27] T. Pant, U. Jain, and H. Wang, *Transported PDF modeling of compressible turbulent reactive flows by using the Eulerian Monte Carlo fields method*, J. Comput. Phys. 425 (2021), 109899.
[28] P. Donde, H. Koo, and V. Raman, *A multivariate quadrature based moment method for LES based modeling of supersonic combustion*, J. Comput. Phys. 231 (2012), pp. 5805–5821.
[29] R. McGraw, *Description of aerosol dynamics by the quadrature method of moments*, Aerosol Sci. Technol. 27 (1997), pp. 255–265.
[30] R.O. Fox, *Computational Models for Turbulent Reacting Flows*, Cambridge University Press, Cambridge, 2003.
[31] C. Yuan, F. Laurent, and R. Fox, *An extended quadrature method of moments for population balance equations*, J. Aerosol Sci. 51 (2012), pp. 1–23.
[32] S. Salenbauch, A. Cuoci, A. Frassoldati, C. Saggese, T. Faravelli, and C. Hasse, *Modeling soot formation in premixed flames using an extended conditional quadrature method of moments*, Combust. Flame 162 (2015), pp. 2529–2543.
[33] E. Madadi-Kandjani, *Quadrature-based models for multiphase and turbulent reacting flows*, Ph.D. diss., Iowa State University, 2017
[34] H. Koo, P. Donde, and V. Raman, *A quadrature-based LES/transported probability density function approach for modeling supersonic combustion*, Proc. Combust. Inst. 33 (2011), pp. 2203–2210.
[35] V. Raman, H. Pitsch, and R.O. Fox, *Eulerian transported probability density function sub-filter model for large-eddy simulations of turbulent combustion*, Combust. Theory Model. 10 (2006), pp. 439–458.
[36] P. Donde, V. Raman, M.E. Mueller, and H. Pitsch, *LES/PDF based modeling of soot-turbulence interactions in turbulent flames*, Proc. Combust. Inst. 34 (2013), pp. 1183–1192.
[37] J. Smagorinsky, *General circulation experiments with the primitive equations: I. The basic experiment*, Mon. Weather Rev. 91 (1963), pp. 99–164.
[38] T. Poinsot and D. Veynante, *Theoretical and Numerical Combustion*, RT Edwards, Inc., 2005.
[39] P.S. Volpiani, *Modèle de plissement dynamique pour la simulation aux grandes échelles de la combustion turbulente prémelangée*, Ph.D. diss., Université Paris-Saclay, 2017
[40] R.G. Gordon, *Error bounds in equilibrium statistical mechanics*, J. Math. Phys. 9 (1968), pp. 655–663.
[41] C. Blumstein and J.C. Wheeler, *Modified-moments method: Applications to harmonic solids*, Phys. Rev. B 8 (1973), pp. 1764–1776.
[42] G. Athanassoulis and P. Gavriliadis, *The truncated Hausdorff moment problem solved by using kernel density functions*, Probab. Eng. Mech. 17 (2002), pp. 273–291.
[43] S.B. Pope, *A Monte Carlo method for the PDF equations of turbulent reactive flow*, Combust. Sci. Technol. 25 (1981), pp. 159–174.
[44] M. Pollack, F. Ferraro, J. Janicka, and C. Hasse, *Evaluation of quadrature-based moment methods in turbulent premixed combustion*, Proc. Combust. Inst. 38 (2021), pp. 2877–2884.
[45] M. Castro, B. Costa, and W.S. Don, *High order weighted essentially non-oscillatory WENO-Z schemes for hyperbolic conservation laws*, J. Comput. Phys. 230 (2011), pp. 1766–1792.
[46] S. Gottlieb and C.W. Shu, *Total variation diminishing Runge–Kutta schemes*, Math. Comput. 67 (1998), pp. 73–85.
[47] S. Gottlieb, C.W. Shu, and E. Tadmor, *Strong stability-preserving high-order time discretization methods*, SIAM Rev. 43 (2001), pp. 89–112.
[48] Z. Lu, H. Zhou, S. Li, Z. Ren, T. Lu, and C.K. Law, *Analysis of operator splitting errors for near-limit flame simulations*, J. Comput. Phys. 335 (2017), pp. 578–591.
[49] F. Hu, *The 6th-order weighted ENO schemes for hyperbolic conservation laws*, Comput. Fluids 174 (2018), pp. 34–45.
[50] E.F. Toro, *Riemann Solvers and Numerical Methods for Fluid Dynamics: A Practical Introduction*, Springer Science & Business Media, 2013.
[51] D. Papamoschou and A. Roshko, *The compressible turbulent shear layer: An experimental study*, J. Fluid Mech. 197 (1988), pp. 453–477.
[52] M. Mungal and P. Dimotakis, *Mixing and combustion with low heat release in a turbulent shear layer*, J. Fluid Mech. 148 (1984), pp. 349–382.
[53] D. Fu and Y. Ma, *Numerical simulation of coherent structure in two-dimensional compressible mixing layers*, Sci. China Ser. A Math. 39 (1996), pp. 1183–1192.

[54] S.K. Lele, *Direct numerical simulation of compressible free shear flows*, in *27th AIAA Aerospace Sciences Meeting*. AIAA Paper 89-0374, 1989

[55] E. George, P. Magre, and V. Sabel'Nikov, *Numerical simulation of self-ignition of hydrogen-hydrocarbons mixtures in a hot supersonic air flow*, AIAA J. 80 (2013), pp. 243–254.

[56] M. Karaca, N. Lardjane, and I. Fedioun, *Implicit large eddy simulation of high-speed non-reacting and reacting air/H2 jets with a 5th order WENO scheme*, Comput. Fluids 62 (2012), pp. 25–44.

[57] J. Li, Z.W. Zhao, A. Kazakov, and F.L. Dryer, *An updated comprehensive kinetic model of hydrogen combustion*, Int. J. Chem. Kinet. 36 (2004), pp. 566–575.